metals

MDPI

Article

On the Plasticity and Deformation Mechanisms in Magnesium Crystals

Konstantin D. Molodov [1], Talal Al-Samman [2] and Dmitri A. Molodov [2,3,*]

[1] Department of Materials and Process Development, Salzgitter Mannesmann Forschung GmbH, Eisenhüttenstr. 99, 38239 Salzgitter, Germany; k.molodov@sz.szmf.de
[2] Institute for Physical Metallurgy and Materials Physics, RWTH Aachen University, 52056 Aachen, Germany; tasamman@imm.rwth-aachen.de
[3] International Research Organization for Advanced Science and Technology (IROAST), Kumamoto University, Kumamoto 860-8555, Japan
* Correspondence: molodov@imm.rwth-aachen.de

Abstract: This work presents an overview of the mechanical response and microstructure evolution of specifically oriented pure magnesium single crystals under plane strain compression at room temperature. Crystals of 'hard' orientations compressed along the *c*-axis exhibited limited room temperature ductility, although pyramidal ⟨c + a⟩ slip was readily activated, fracturing along crystallographic $\{11\bar{2}4\}$ planes as a result of highly localized shear. Profuse $\{10\bar{1}2\}$ extension twinning was the primary mode of incipient deformation in the case of orientations favorably aligned for *c*-axis extension. In both cases of compression along $\langle 11\bar{2}0\rangle$ and $\langle 10\bar{1}0\rangle$ directions, $\{10\bar{1}2\}$ extension twins completely converted the starting orientations into twin orientations; the subsequent deformation behavior of the differently oriented crystals, however, was remarkably different. The formation of $\{10\bar{1}2\}$ extension twins could not be prevented by the channel-die constraints when *c*-axis extension was confined. The presence of high angle grain boundaries and, in particular, $\{10\bar{1}2\}$ twin boundaries was found to be a prerequisite for the activation of $\{10\bar{1}1\}$ contraction twinning by providing nucleation sites for the latter. Prismatic slip was not found to operate at room temperature in the case of starting orientations most favorably aligned for prismatic slip; instead, cooperative $\{10\bar{1}2\}$ extension and $\{10\bar{1}1\}$ contraction twinning was activated. A two-stage work hardening behavior was observed in 'soft' Mg crystals aligned for single or coplanar basal slip. The higher work hardening in the second stage was attributed to changes in the microstructure rather than the interaction of primary dislocations with forest dislocations.

Keywords: magnesium; single crystal; deformation twinning; plasticity

Citation: Molodov, K.D.; Al-Samman, T.; Molodov, D.A. On the Plasticity and Deformation Mechanisms in Magnesium Crystals. *Metals* **2023**, *13*, 640. https://doi.org/10.3390/met13040640

Academic Editor: Qingshan Yang

Received: 12 February 2023
Revised: 9 March 2023
Accepted: 21 March 2023
Published: 23 March 2023

1. Introduction

Magnesium is the lightest structural metal, about one-third lighter than aluminum, and it has less than one-quarter of the density of ferrous alloys. Moreover, magnesium has a high specific strength and stiffness as well as high damping properties compared to other metals. It is abundantly available in the earth's crust and seawater and has a high recyclability. Magnesium alloys are also superior at electromagnetic interference shielding, which makes them well suited for housings of portable electronic consumer goods. However, while cast magnesium is widely utilized, there are a number of technical difficulties hampering the large-scale use of wrought magnesium alloys.

Generally, magnesium sheets have a poor formability at room temperature, which is improved markedly above 175 °C [1]. During the primary fabrication process, e.g., rolling, grains rotate to unfavorable orientations (strong texture) for isotropic plasticity [2]. Further processing steps must therefore be carried out at elevated temperature to thermally activate additional modes of deformation, which leads to high production costs. Further issues that limit the applicability of wrought magnesium are a strong yield asymmetry [3] due to

deformation twinning, edge-cracking in rolling and a low ductility at high strength [4] as well as poor corrosion resistance [2].

No matter whether the difficulties associated with the poor ductility of wrought magnesium at ambient temperature will be overcome by innovative processing, alloy and/or microstructure design, understanding the underlying physical mechanisms and microstructural changes in the material during processing is paramount.

A lot of research effort was dedicated to uncovering the operating modes of deformation in magnesium. Well-known studies on magnesium single crystals were performed by Wonziewicz and Backofen [5] as well as by Kelly and Hosford [6] in the 1960s. Both studies included plane strain compression tests on differently oriented magnesium single crystals, demonstrating their complex deformation behavior, which is characterized by profuse deformation twinning and the occurrence of recrystallization. However, the investigations mentioned above were limited to rather small strains as their focus was on the temperature dependence of slip and twinning activation. Following these classical works, there was surprisingly little incentive to characterize the deformation behavior of Mg single crystals, despite the apparent need for reliable modeling based on real physical mechanisms. Hence, the lack of a holistic understanding of the deformation behavior, microstructure and texture evolution in Mg single crystals calls for a reexamination of the fundamental underlying mechanisms, especially considering the advent of more advanced characterization techniques and general progress in research.

Compared to investigations of polycrystals, studies on single crystals claim several advantages. Single crystals can be precisely oriented with respect to the loading axes, which allows one to target and isolate specific modes of deformation, especially in conjunction with imposed constraints. Furthermore, model case experiments on single crystals provide an opportunity to examine the deformation behavior, microstructure and texture evolution depending on the initial orientation of the crystal. The operating slip modes and the critical resolved shear stress (CRSS) can be readily determined. Multiple generations of deformation twins can be easily distinguished even when the typical twin morphology is lost, which is rarely possible in polycrystals. The emergence of new grains and their orientation relationship to the surrounding matrix can be readily traced, which can grant valuable insight in the mechanisms of recrystallization [7]. In general, the use of single crystals permits a much clearer and forthright analysis of the observed microstructural changes compared to conventional studies on polycrystals.

In light of these advantages of studies employing single crystals, it is imperative to note that, in general, individual grains in a polycrystal do not deform as single crystals. This is especially true for metals with crystal structures of high symmetry where multiple slip is prevalent. Single crystal studies therefore aim at exposing the underlying physical mechanisms, rather than claiming to directly predict the deformation behavior of polycrystals. That said, in the case of magnesium, very strong basal textures are predominant; hence, individual grains often undergo a similar deformation compared to what is tested in single crystal studies, especially when constraints are used. Furthermore, the small number of independent deformation modes, i.e., the dominance of basal slip and extension twinning at room temperature, entails a deformation behavior of the polycrystal that can be approximated by a Sachs-type model [8–10], in which the operation of only one deformation mode per grain is assumed. To this end, understanding the deformation behavior of single crystals is indispensable.

Deformation of Mg at room temperature is particularly arduous owing to only a limited number of slip and twinning systems that can be activated to accommodate the imposed deformation. Plastic anisotropy is greatly pronounced, i.e., crystals of varying orientations are expected to exhibit a drastically different mechanical response (see, for example [11,12]). Performing model case experiments on specifically oriented single crystals allows to isolate and to identify the mechanisms of deformation, which in turn yields valuable insight in the deformation behavior of polycrystalline Mg.

The aim of the present work is to provide an overview of the mechanical response and microstructure evolution of specially oriented pure Mg single crystals during plane strain compression at room temperature in order to expose the mechanism involved. Special emphasis is placed on the investigation of crystal orientations in which basal slip is inhibited initially since that provides an opportunity to focus on non-basal slip systems and deformation twinning more exclusively. Furthermore, the critical resolved shear stress of slip and twinning, the work hardening and the fracture behavior are characterized.

2. Specimens and Applied Methods to Study Deformation of Mg Single Crystals

2.1. Single Crystal Growth

Mg of commercial purity (99.98%) was used as the starting material for pure Mg crystals. Cylindrical crystal seeds (∅ 5 mm × 25 mm) with the *c*-axis aligned parallel to the axis of symmetry (maximum angular deviation of 0.2°) were cut from a randomly oriented single crystal by electrical discharge machining (EDM) [13] in order to avoid any plastic deformation of the material. EDM was performed using a wire with a diameter of 0.25 mm.

The crystal seeds were etched in a 5% solution of nitric acid and boiled in distilled water for several minutes in order to form a stable oxide layer on the surface. The same procedure was done for a polycrystalline blank. The oxide layer acted as a barrier between the molten Mg and the inside of the mold, preventing diffusion and adherence. After preparation, the crystal seed and the blank were placed in a cylindrical steel mold. While the top part of the mold was made from stainless steel, the steel used for the bottom part that was in contact with the molten Mg did not contain any Ni to prevent contamination. A graphite-based die coating (Acheson Hydrokollag IP 5) was used to cover the inside of the mold.

For the growth of oriented single crystals by direct solidification the Bridgman method [14] in a vertical configuration was utilized. The resulting crystals had a conical shape with a base diameter of 34 mm, a length of 56 mm and an opening angle of 4° (Figure 1a).

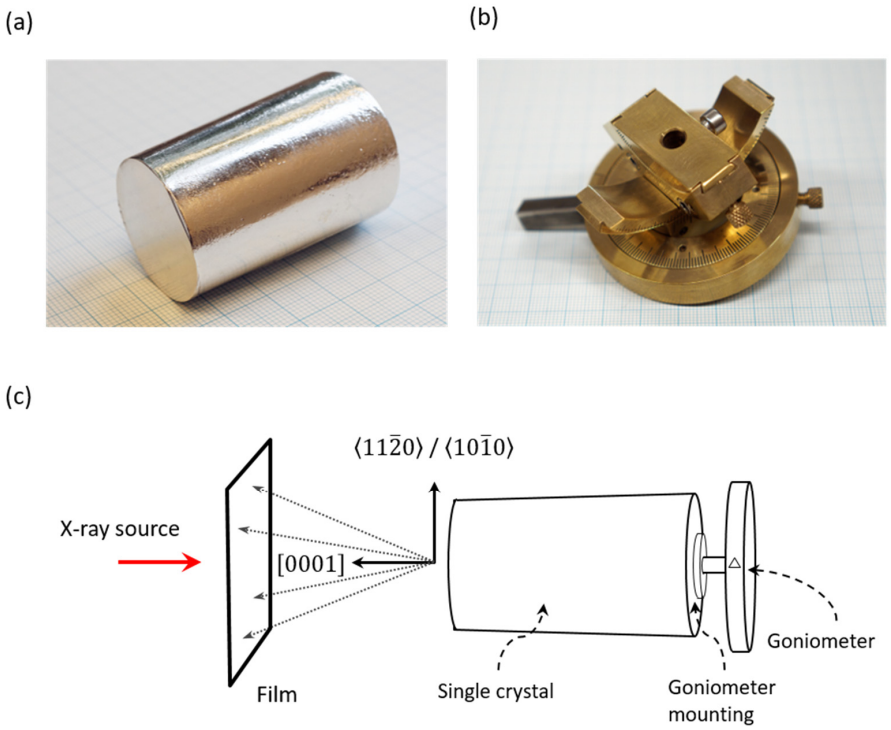

Figure 1. (**a**) Conically shaped pure Mg single crystal (etched in dilute nitric acid) with the *c*-axis nearly parallel to the axis of symmetry (millimeter paper for scale); (**b**) 3-axis goniometer used for alignment of the single crystals and (**c**) schematic illustration of a single crystal mounted on a goniometer and aligned according to the desired orientation of the final specimens using Laue (white beam) X-ray backscatter diffraction.

A brass goniometer mounting was adhered to the back end of each crystal using glue mixed with copper powder to ensure conductivity during EDM (when the crystal was mounted onto a goniometer). Each grown single crystal was attached to a 3-axis goniometer (Figure 1b) and aligned according to the desired final orientation of the specimens using the Laue X-ray back-diffraction method detailed in Ref. [15] (Figure 1c). After alignment, specimens were cut for mechanical testing.

2.2. Channel-Die Plane Strain Compression Tests

Mg single crystals were subjected to plane strain compression (PSC) testing using a channel-die as shown in Figure 2a. For the PSC tests, cuboid specimens with dimensions of 14 mm × 10 mm × 6 mm were fabricated by means of EDM from the specially oriented single crystals. A schematic illustration of the channel-die device with respect to the specimen axes is shown in Figure 2b. Extension was limited to the longitudinal direction (LD) since extension in the transverse direction (TD) was suppressed by the channel-die walls. Mechanical tests were carried out at room temperature and a constant strain rate of 10^{-3} s^{-1} by means of a conventional screw-driven ZWICK 1484 testing machine.

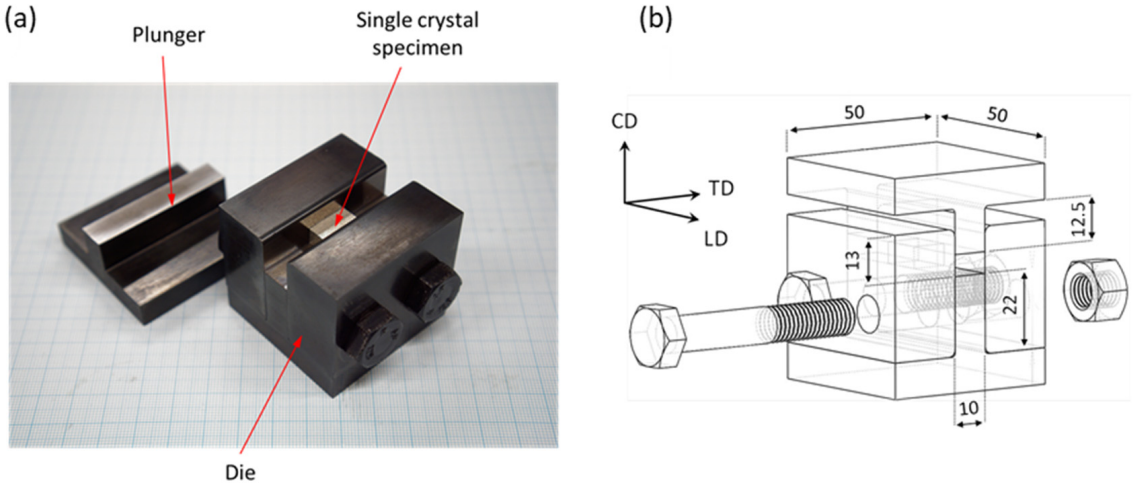

Figure 2. (**a**) Channel-die device used for plane strain compression tests with a Mg specimen; (**b**) schematic illustration of the channel die in (**a**) (LD—longitudinal direction, TD—transverse direction, CD—compression direction). Measurements are given in mm.

The specimens were strained up to various logarithmic (true) strains, defined by $\varepsilon_t = \ln(1+\varepsilon)$, where ε is the engineering strain. The applied force and displacement in the CD were both monitored and automatically controlled by a computer with a data acquisition system. The preloading force was 50 N, which translates into 0.36 MPa. To reduce friction, hydraulic oil was used for lubrication.

Single crystals with different ideal orientations, including compression along (orientations A and B) and perpendicular to the *c*-axis (orientations C–F) as well as orientations with the *c*-axis inclined at an angle of 45° to the compression direction (orientations G and H), were tested in plane strain compression. The mismatch between the crystallographic directions and the specimen axes, i.e., compression (CD), longitudinal (LD) and transverse direction (TD) of the channel die, was less than 1°. An overview of the ideal specimen orientations is given in Table 1 expressed as $(\varphi_1, \Phi, \varphi_2)$ in Euler space.

Table 1. Orientations of single crystal specimens deformed by plane strain compression in a channel-die. (Quotation marks indicate irrational directions with rounded indices). Euler angles are expressed as (φ_1, Φ, φ_2) in Euler space (in Bunge notation, with x | | [$0\bar{1}10$] and y | | [$2\bar{1}\bar{1}0$]). The deviation from the ideal orientations was less than 1°.

Single Crystal Orientations	Euler Angles (°)	Crystal Direction in		
		LD	TD	CD
A	(0 0 90)	$[\bar{2}\,1\,1\,0]$	$[0\,\bar{1}\,1\,0]$	[0 0 0 1]
B	(0 0 0)	$[0\,\bar{1}\,1\,0]$	$[2\,\bar{1}\,\bar{1}\,0]$	[0 0 0 1]
C	(90 90 0)	[0 0 0 1]	$[0\,\bar{1}\,1\,0]$	$[2\,\bar{1}\,\bar{1}\,0]$
D	(90 90 90)	[0 0 0 1]	$[\bar{2}\,1\,1\,0]$	$[0\,\bar{1}\,1\,0]$
E	(0 90 0)	$[0\,\bar{1}\,1\,0]$	$[0\,0\,0\,\bar{1}]$	$[2\,\bar{1}\,\bar{1}\,0]$
F	(0 90 90)	$[\bar{2}\,1\,1\,0]$	$[0\,0\,0\,\bar{1}]$	$[0\,\bar{1}\,1\,0]$
G	(90 45 0)	′$[\bar{1}\bar{2}\,6\,6\,11.1]$′	$[0\,\bar{1}\,1\,0]$	′$[12\,\bar{6}\,\bar{6}\,11.1]$′
H	(90 45 90)	′$[0\,11.2\,\bar{1}\bar{1}.\bar{2}\,12]$′	$[\bar{2}\,1\,1\,0]$	′$[0\,\bar{1}\bar{1}.\bar{2}\,11.2\,12]$′

2.3. Sample Preparation

Metallographic sample preparation included soft grinding on grinding discs with 1200, 2400 and 4000 grit SiC-paper. Ethanol was used for lubrication/cooling in the final grinding step instead of water to avoid oxidation. Grinding was followed by 3 and 1 µm diamond polishing on Struers MD-Nap cloths at a very low rotation speed using an oil-based and water-free coolant until scratches could not be recognized visually. After diamond polishing, electropolishing in a 5:3 solution of ethanol and H_3PO_4 at 2 V was performed. Average electropolishing times were about 1 h. In some cases, e.g., channel-die specimens of orientation F, electropolishing times of up to 4 h were required to yield satisfying results, i.e., a deformation and twin free surface. Comparatively long electropolishing times were necessary since single crystalline Mg samples were particularly prone to deformation twinning during sample preparation (i.e., mechanical grinding and polishing). Electropolishing was performed at all times, irrespective of the characterization technique used, e.g., optical microscopy or electron backscatter diffraction. Extremely careful handling of specimens was crucial to avoid deformation of the soft single crystals. The deformed specimens after PSC tests were etched in a 5% solution of nitric acid, cut at the mid-surface of the LD-TD plane by EDM and prepared for further characterization. Chemical color-etching with a freshly prepared 1:1:7 solution of water, acetic acid and picral (4% picric acid in solution with ethanol) was performed for optical microscopy investigations using polarized light.

2.4. Characterization Techniques

Microstructure characterization using polarized light was performed on a Zeiss Axio Imager A1m optical microscope. Furthermore, C-DIC (circular polarized light-differential interference contrast) [16] was applied to characterize the microstructure and surface topology. Micrographs (between 50 and 300 images per sample) covering the whole specimen surface were acquired manually at low magnifications and stitched together using a specially developed in-house software (utilizing the scale-invariant feature transform algorithm by David Lowe [17]) to obtain a complete high-resolution macroscopic image of the investigated plane. Supplementary stereomicroscopy was performed on a Zeiss Discovery V12 optical microscope fitted with variable LED illumination to provide orientation-dependent information on the surface topology at low magnifications, albeit without offering color contrast.

The Laue (back-reflection) technique was used to measure the orientations of single crystals (see Section 3.1) by placing a film between the X-ray source (W-tube operating at 45 kV and 30 mA) and the measured specimen. The positions of Laue-reflections (spots) on the film were determined using magnified scans of the Laue micrographs and indexed

using the software 'OrientExpress 3.4' by J. Laugier (Laboratoire des Materiaux et du Génie Physique de l'Ecole Supérieure de Physique de Grenoble).

Electron backscatter diffraction (EBSD) measurements were performed using a scanning electron microscope (SEM) equipped with a field emission gun (Leo Gemini 1530 with a LaB_6 filament) and an HKL-Nordlys II EBSD detector to characterize the microstructure and microtexture. The samples were mounted onto custom machined brass holders to ensure a perfect alignment and tilted to 70° (from the horizontal) towards the EBSD detector to increase the backscattering yield. An acceleration voltage of 20 kV was used for all measurements. The Matlab toolbox MTEX [18,19] was utilized to analyze and visualize the EBSD data, including correction of the EBSD raw data (filtering based on a maximum mean angular deviation and nearest neighbor extrapolation) and grain reconstruction.

3. Plastic Response and Microstructure of Differently Oriented Mg Single Crystals

3.1. Flow Behavior of Mg Single Crystals

As shown in Figure 3, the investigated pure Mg single crystal specimens with different initial orientations exhibited very different mechanical behavior during ambient temperature PSC deformation. The four orientations A, C, E and G (Figure 3a) shared a 30° rotation around their respective *c*-axes with the orientations B, D, F and H (Figure 3b). For instance, in the case of orientations A and B, the imposed deformation yielded contraction along the *c*-axis while extension was confined to the crystallographic $\langle 11\bar{2}0\rangle$ and $\langle 10\bar{1}0\rangle$ directions, respectively. Orientations C and D represented the case of *c*-axis extension, whereas the *c*-axis extension was confined for the orientations E and F (*c*-axis parallel to TD). Orientations G and H were the only ones that were aligned for basal slip. For all other orientations, the basal plane was either parallel or perpendicular to the compression direction, i.e., basal slip was suppressed.

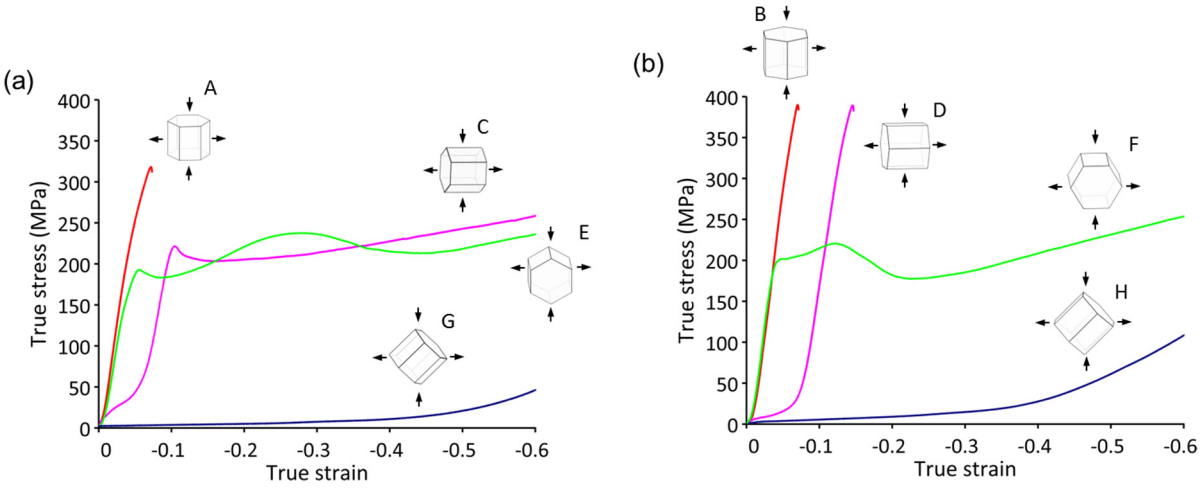

Figure 3. Flow curves of the investigated pure Mg single crystal specimens of various orientations deformed by PSC at ambient temperature and a constant strain rate of 10^{-3} s^{-1}. Oil was used for lubrication. The same colors are used to denote orientations that share a 30° rotation around their respective *c*-axis in (**a**,**b**).

Specimens of orientations A (Figure 3a) and B (Figure 3b), i.e., the case of *c*-axis contraction, displayed the least ductility at room temperature, reaching a maximum true strain of −7.3% and −6.6%, respectively, at fracture. Crystals of other orientations were significantly more ductile, reaching a true strain of −1, with the exception of orientation D, the flow behavior of which was more similar to that of orientation B (Figure 3b) than its counterpart orientation C (Figure 3a).

Apart from crystals of orientations C and D that showed a highly diverse deformation behavior in *c*-axis extension, the stress-strain curves for the other orientations were

qualitatively similar when compared to their counterparts (rotated by 30°). However, quantitatively, significant differences were apparent. In other words, no single crystal tested displayed the exact same deformation behavior as another one with a different orientation, demonstrating the great extent of plastic anisotropy in Mg.

3.2. Contraction along the c-Axis (Orientations A and B)

The flow curves for specimens of orientations A and B are shown in Figure 4. Basal slip was suppressed in both cases. Initial strain hardening rates were among the highest compared to other orientations. The hardening rates $d\sigma_t/d\varepsilon_t$ for specimens of orientation A and B were determined to be 6.3 GPa and 6.9 GPa, respectively, in the initial linear region of the flow curves. However, the hardening rates decreased at higher strains, most notably seen in the case of orientation A (Figure 4). The hardening rates $d\sigma_t/d\varepsilon_t$ measured in the linear regions of the flow curves prior to fracture were 3.2 GPa for orientation A and 5.5 GPa for orientation B.

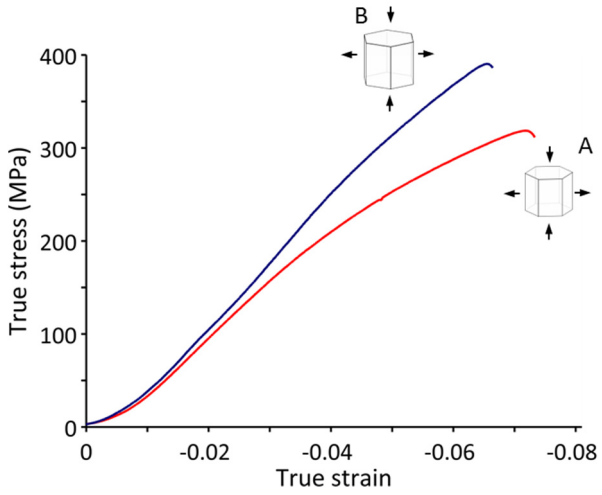

Figure 4. Flow curves of pure Mg single crystals of orientations A and B (*c*-axis contraction) deformed by PSC at ambient temperature and a constant strain rate of 10^{-3} s^{-1}. Oil was used for lubrication.

For both orientations A and B, fracture always occurred along $\{11\bar{2}4\}$ planes repeatedly, as seen in Figure 5. The specimens typically cracked in a rather violent event that caused pieces to break off as shown in Figure 5b. The maximum true stress attained was 320 MPa and 390 MPa for orientation A and B, respectively. Right before fracture occurred, the flow curves exhibited an inflection point, followed by a continuous brief decrease in flow stress.

Specimens of orientation A that were polished prior to testing and strained without exceeding the rupture stress revealed the existence of slip traces. Slip traces on the CD-TD plane (the only unconstrained plane in channel-die compression) are shown in Figure 6. Fine horizontal traces (Figure 6a) as well as fine diagonal lines at an angle of 54–57° to TD (Figure 6b) and coarser diagonal bands (Figure 6c) in a diamond-like pattern were present. These slip lines were found to be nearly parallel to traces of $\{11\bar{2}2\}$ planes (Figure 6). It is worth noting that the horizontal lines depicted in Figure 6a could have also originated from slip on the basal plane; however, basal slip could not account for the appearance of diagonal lines on the CD-TD surface of A-orientated crystals (Figure 6b).

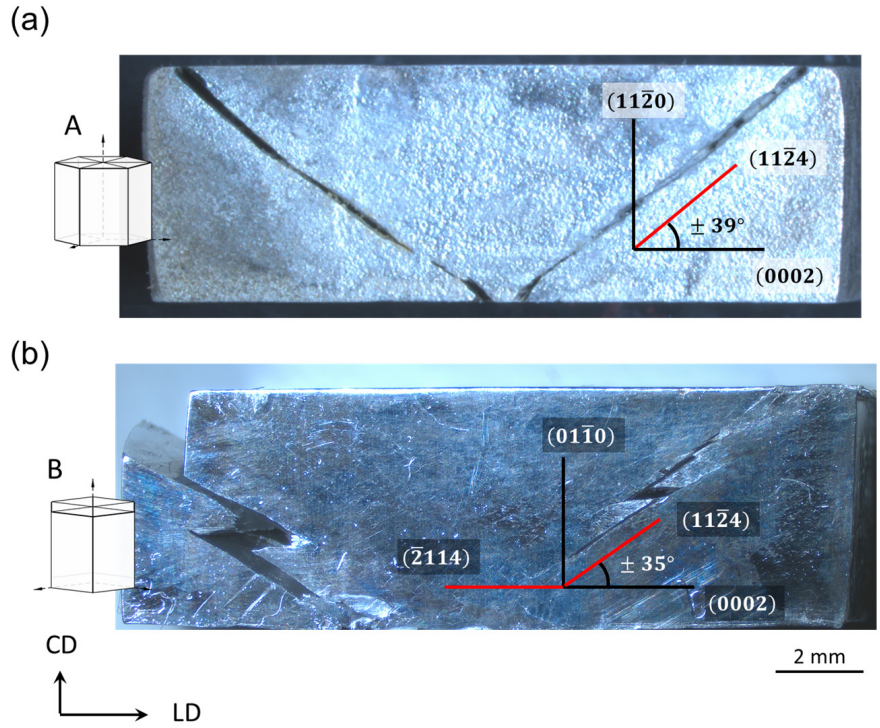

Figure 5. Optical micrographs of the CD-LD plane of a specimen with (**a**) initial orientation A and (**b**) initial orientation B after fracture at room temperature.

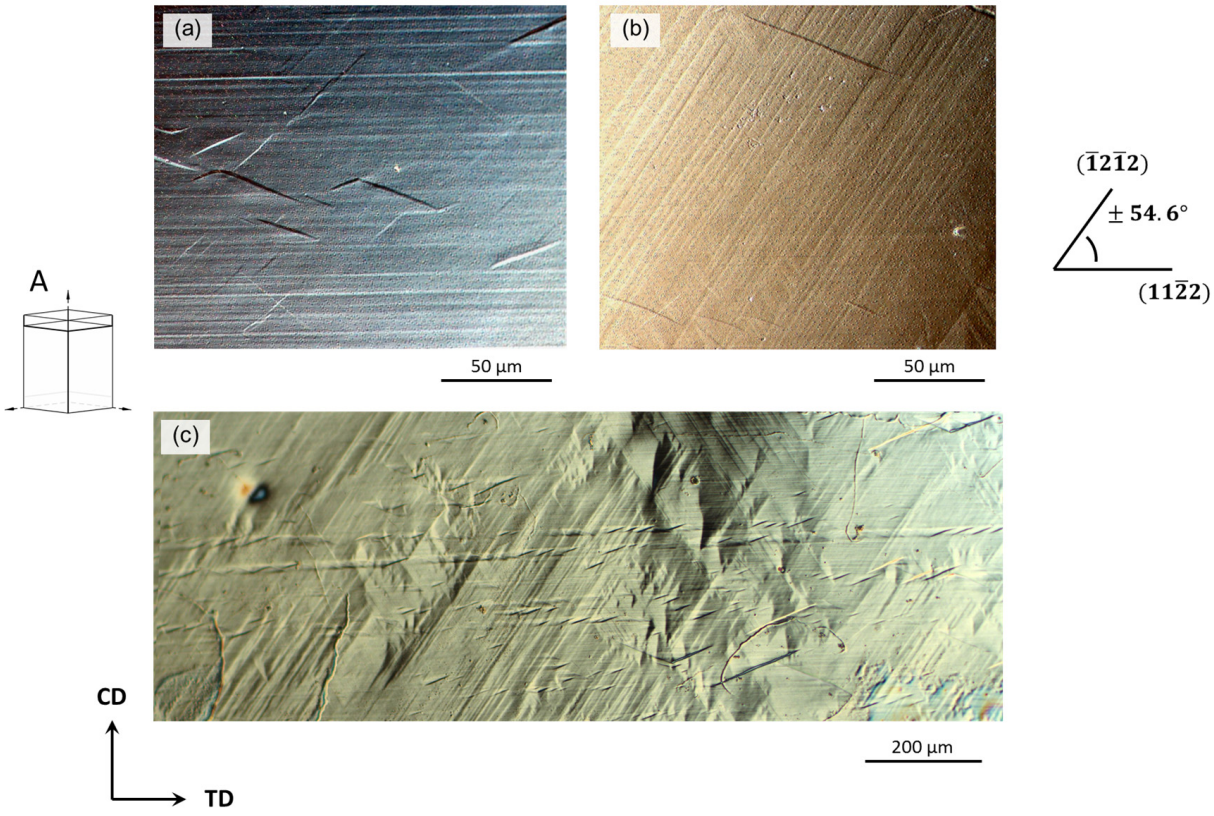

Figure 6. Optical micrographs (C-DIC) of a prepolished CD-LD side of a specimen with the initial orientation A showing (**a**) horizontal slip traces, (**b**) fine diagonal slip traces and (**c**) rutted surface with a diamond-like slip pattern.

The CD-LD surface of specimens with orientation B was significantly more rutted compared to those with orientation A. Like in the case of orientation A, horizontal slip lines were apparent. Non-rectilinear diagonal slip traces were observed as well at inclinations in a brought range of 43–58° to TD (Figure 7). These traces could not be clearly assigned to a particular slip plane; however, they were not a result of basal slip.

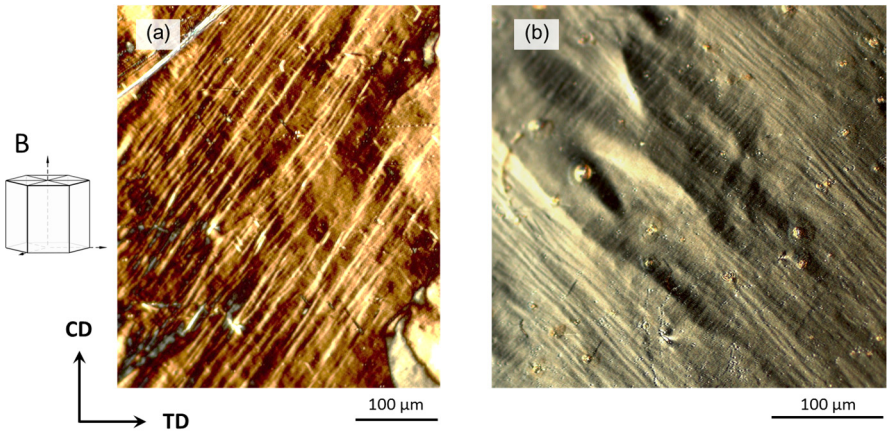

Figure 7. Optical micrographs (C-DIC) of a prepolished CD-LD side of a specimen with starting orientation B showing non-rectilinear diagonal slip traces at an angle of (**a**) approximately 55° and (**b**) approximately 46° to TD.

Besides slip lines, numerous $\{10\bar{1}2\}$ extension twins were frequently observed on the CD-LD surface of specimen A and B despite the imposed *c*-axis contraction. However, their appearance must be attributed to inhomogeneous flow during unloading and the corresponding residual stresses [5,20].

Detailed examination of the failed samples (orientation B) revealed the presence of narrow recrystallized bands nearly parallel to the trace of $\{11\bar{2}4\}$ planes (planes of fracture) on the TD-LD surface (Figure 8). The matrix orientations adjacent to the band in Figure 8 (left and right) were rotated away from the initial orientation of the single crystal in different directions about an axis parallel to the band, leading to a misorientation angle of up to 8° between them, i.e., local splitting of the initial basal texture occurred. At other bands (not shown here) splitting of up to 30° was observed. Cracks were either directly evident in such bands, mostly along grain boundaries (Figure 8a), or these bands continued into cracked regions (Figure 8b). An orientation map of the recrystallized band in Figure 8b is shown in Figure 8c. A larger number of $\{10\bar{1}2\}$ extension twins were often found in the vicinity of such cracked/recrystallized bands (blue in Figure 8c); however, $\{10\bar{1}1\}$ or $\{11\bar{2}4\}$ contraction twins were not observed. Moreover, the grains in the band interior did not harbor any indication that the band was a former $\{11\bar{2}4\}$ twin, although this is suggested by the $\{11\bar{2}4\}$ trace of the band. None of the grains had a misorientation (with respect to the matrix) close to that of a $\{11\bar{2}4\}$ twin, which would be 78.14° around $\langle\bar{1}100\rangle$.

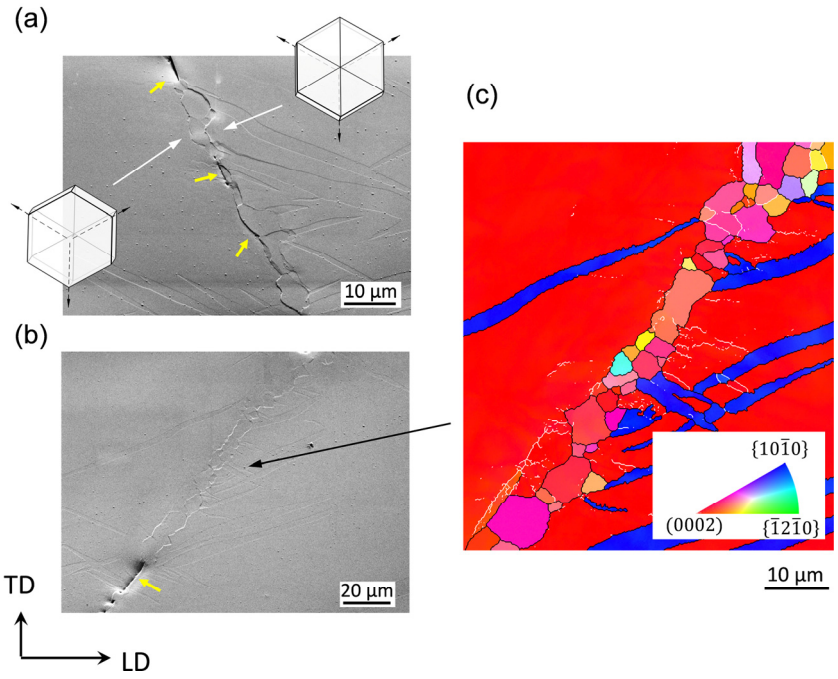

Figure 8. (**a**,**b**) SEM micrographs of recrystallized bands and cracks on the TD-LD surface and (**c**) orientation map of the band in (**b**) in inverse pole figure (IPF) coloring with respect to CD. Yellow arrows in (**a**,**b**) indicate cracks.

3.3. Extension along the c-Axis (Orientations C and D)

As mentioned above (in Section 3.1), the flow behavior of C- and D-oriented crystals in *c*-axis extension was distinctively different. The respective stress–strain curves at room temperature are depicted in Figure 9. Specimens of orientation D failed at a true strain of −14.7%, whereas samples with the starting orientation C showed extraordinary high room temperature ductility and deformed up to a true strain of −100%. Analogous to the case of orientation A and B, basal slip was suppressed for both starting orientations C and D due to the alignment of the basal planes with respect to the compression direction. The incipient stage of deformation was characterized by a low strain hardening rate ($d\sigma_t/d\varepsilon_t$) of 544 MPa and 297 MPa for orientations C and D, respectively. However, at strains above −5%, the initial region of low work hardening was followed by a linear hardening region with significantly higher strain hardening rates of 4.6 GPa and 5.6 GPa for orientation C and D, respectively. The rapid hardening region was interrupted by a sudden continuous drop in flow stress in the case of orientation C at a true stress of 220 MPa and a true strain of −10.5%, after which the flow stress remained steady up to a true strain of −20%. No such drop in flow stress was witnessed for orientation D. Instead, the rapid work hardening continued until fracture. It is worth noting that the fracture stress and hardening rate in the rapid work hardening regime of orientation D was nearly identical to that of orientation B (*c*-axis contraction) (Figure 3).

With respect to the microstructure evolution, profuse $\{10\bar{1}2\}$ extension twinning was observed during early stages of deformation (Figure 10). $\{10\bar{1}2\}$ extension twins consumed about half of the matrix at a true strain of −3% for both C- (Figure 10a) and D-oriented specimens (Figure 10b). In addition to those twins, secondary $\{10\bar{1}2\}$ extension twins were also found inside the primary ones in C-oriented crystals (inset in Figure 10a).

A major difference in the behavior of specimens with the initial orientations C and D at this point was in the selected twin variants. For orientation C, the TD–LD (primary) twin traces were at an angle of ±65° to LD (Figure 10a), while for orientation D, the traces of the twinning planes were parallel to TD, as evident from the twin trace in Figure 10b. The twin orientations that were obtained by EBSD measurements are illustrated in Figure 11. In the case of orientation C (Figure 11a), the basal poles of the $\{10\bar{1}2\}$ extension twin orientations

were about 30° away from the center of the basal pole figure (compression direction). By contrast, the twin orientations that originated from orientation D were located right in the center of the basal pole figure (Figure 11b).

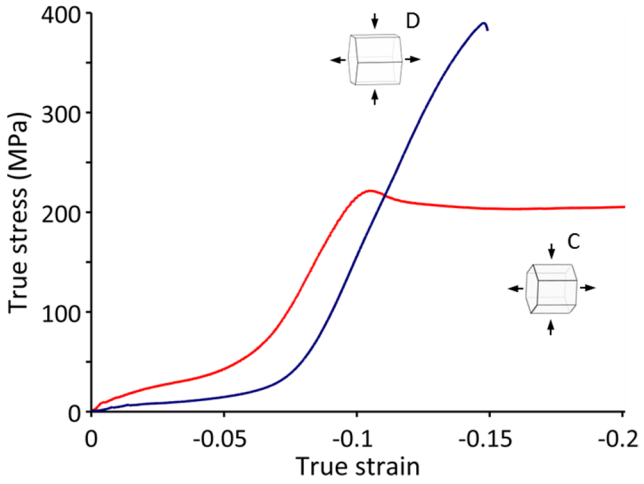

Figure 9. Flow curves of pure Mg single crystals of orientations C and D (*c*-axis extension) deformed by PSC at ambient temperature and a constant strain rate of 10^{-3} s^{-1}. Oil was used for lubrication.

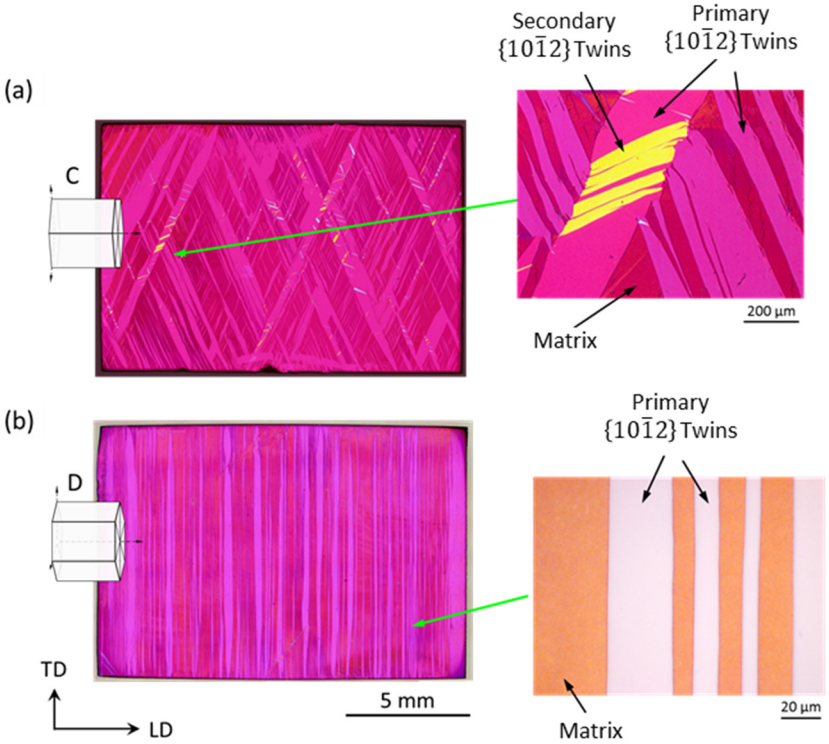

Figure 10. Optical micrographs of the whole specimen mid-thickness plane after PSC tests at a true strain of −3% at room temperature of crystals with (**a**) orientation C and (**b**) orientation D.

At slightly higher strains, the respective primary twins completely consumed the initial single crystal matrix of orientation C (Figure 12a) and D (Figure 12b), i.e., the starting orientations C and D were completely converted into twin orientations. At the peak stress on the flow curve for orientation C, secondary $\{10\bar{1}2\}$ extension and, more importantly, $\{10\bar{1}1\}$ contraction twins were evident. (For an in-depth description of the deformation behavior of C-oriented crystals at higher strains, the reader is referred to Ref. [21].) No $\{10\bar{1}1\}$ contraction twins were seen to form in the case of orientation D. Specimens of

orientation D effectively turned into single crystals after primary twinning (Figure 12b). The orientation of the new matrix (Figures 11b and 13) was nearly identical to that of orientation B (*c*-axis contraction), i.e., the *c*-axis was parallel to CD and a crystallographic $\langle 10\bar{1}0 \rangle$ direction was parallel to LD. However, strictly speaking, the specimens were not fully single-crystalline but comprised low angle (<8°) boundaries parallel to TD (Figure 13a) and orientation gradients up to approximately 4°, resembling the morphology of the twins that consumed the initial matrix (Figure 13b).

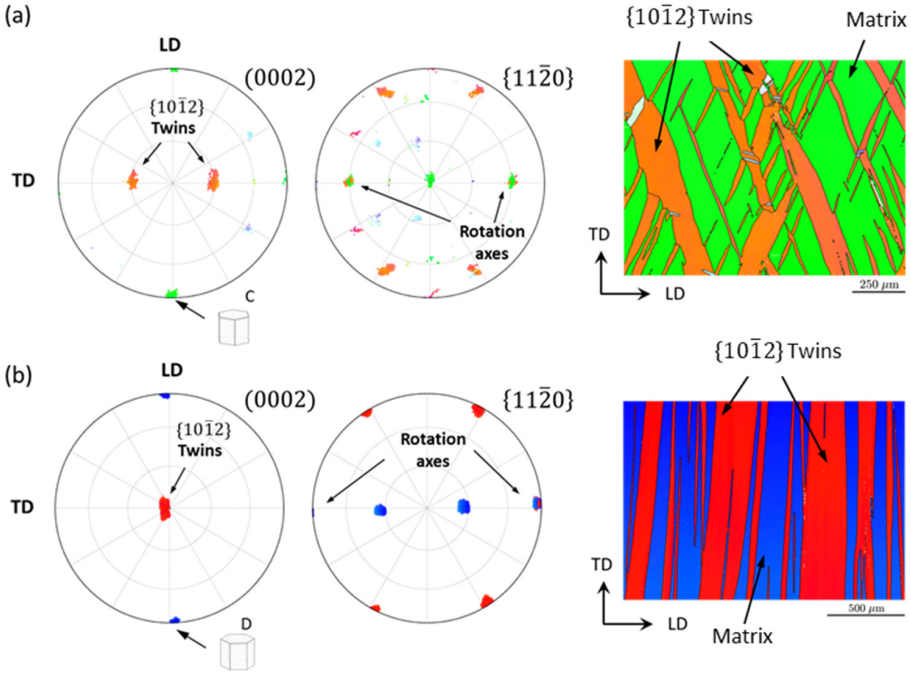

Figure 11. Discrete (scatter) pole figures and corresponding orientation maps for (**a**) orientation C and (**b**) orientation D at a true strain of −3%.

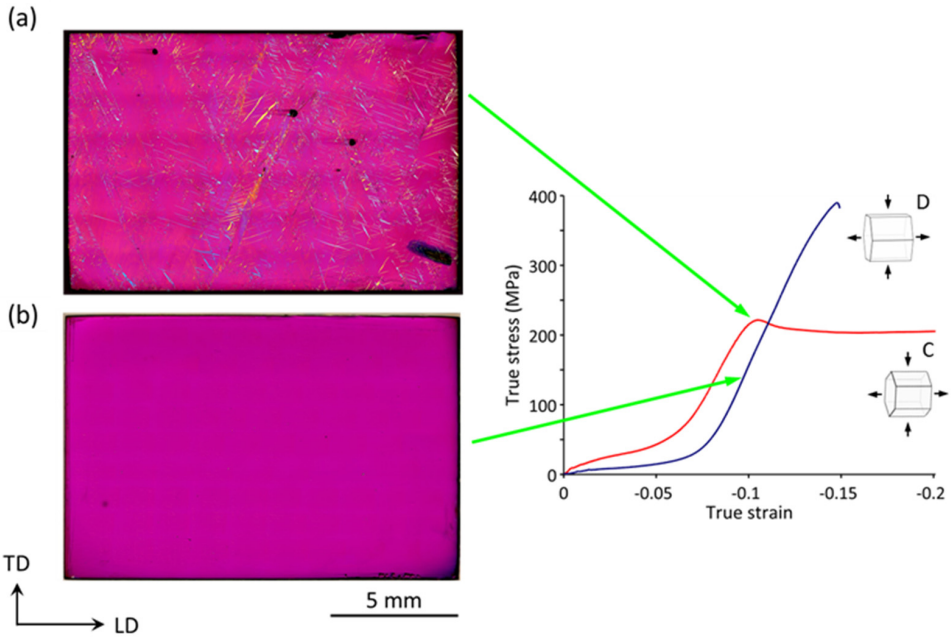

Figure 12. Optical micrographs of the whole specimen mid-thickness plane after PSC tests at room temperature of crystals with (**a**) orientation C at a true strain of −11% and (**b**) orientation D at a true strain of −10.5%.

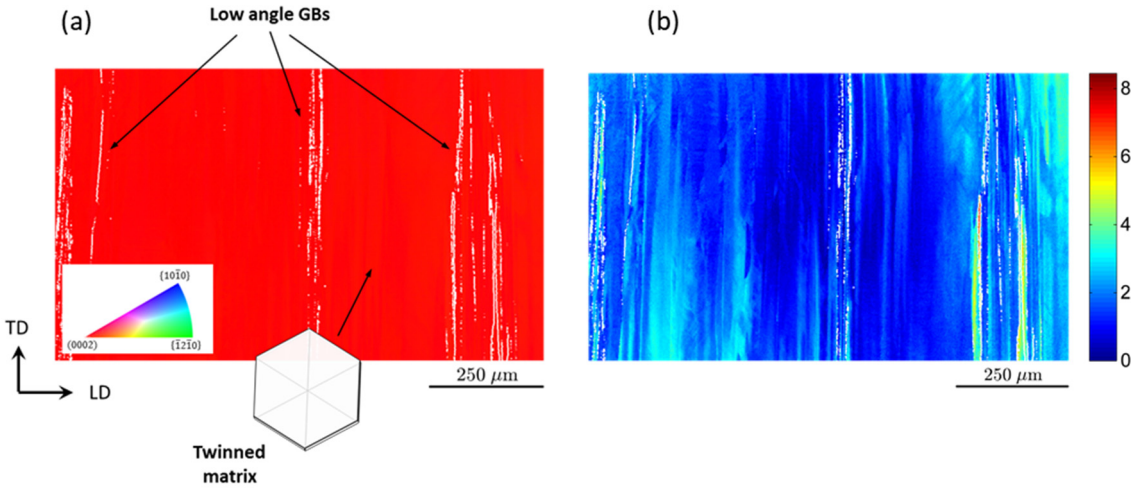

Figure 13. (**a**) Orientation map of a specimen of orientation D from Figure 12b ($\varepsilon_t = -10.5\%$). White lines represent low angle grain boundaries (GBs). (**b**) Grain Reference Orientation Deviation in [°] for the map in (**a**).

3.4. Constrained c-Axis (Orientations E and F)

Orientations E and F were both aligned favorably for prismatic slip. Basal slip was suppressed as well as $\{10\bar{1}2\}$ extension twinning since the *c*-axis was parallel to TD in both orientations. The stress–strain response of E- and F-oriented crystals is presented in Figure 14 for a true strain up to −10%. Specimens were deformed up to −100% without failing, although cracks were evident at intermediate strains as already reported and discussed in [22]. The initial mechanical response was of a sigmoidal type, governed by a rapid increase in flow stress. The linear strain hardening rates $d\sigma_t/d\varepsilon_t$ were 5.5 GPa and 6.8 GPa for orientation E and F, respectively, in the initial rapid hardening stage (between a true strain of −1% and −3%). It is worth pointing out that the initial hardening rate of orientation F was very similar to that of orientation B (6.9 GPa), as can also be seen in Figure 3b (green and red flow curves). After reaching a flow stress of 193 MPa and 202 MPa in the case of orientation E and F, respectively, a drastic change in work hardening behavior was evident—similar to what was observed for orientation C (Figure 9). Up to a true strain of −10%, the flow stress in both cases (orientation E and F) remained nearly steady.

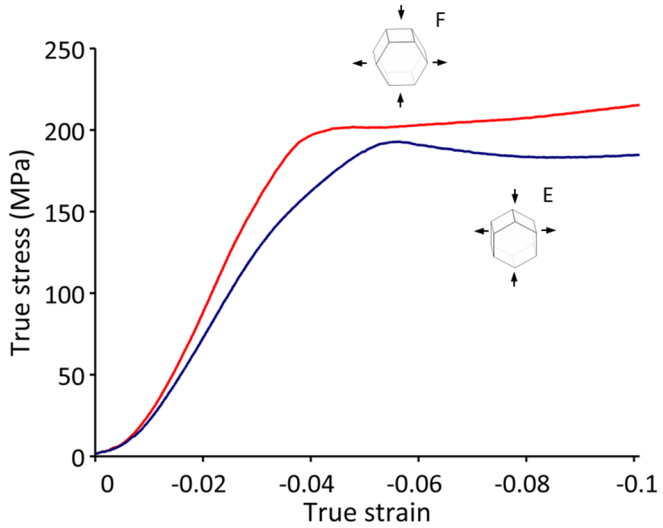

Figure 14. Flow curves of pure Mg single crystals of orientations E and F (constrained *c*-axis) deformed by PSC at ambient temperature and a constant strain rate of 10^{-3} s^{-1}. Oil was used for lubrication.

Although extension along the *c*-axis was confined by the channel-die walls, $\{10\bar{1}2\}$ extension twins were observed to form in the initial regime of rapid work hardening in both cases of orientation E (Figure 15a) and F (Figure 15b) at a true strain of −3%. Since some minimal leeway was present between the samples and the channel-die walls (in order to be able to place the sample in the channel die), it was attempted to further suppress the extension in TD by inserting a slightly wider sample prior to assembling and tightening the channel-die, i.e., a preloading force was applied in TD; hence, there was no room for extension of the sample in TD. Nevertheless, $\{10\bar{1}2\}$ extension twins were observed to form.

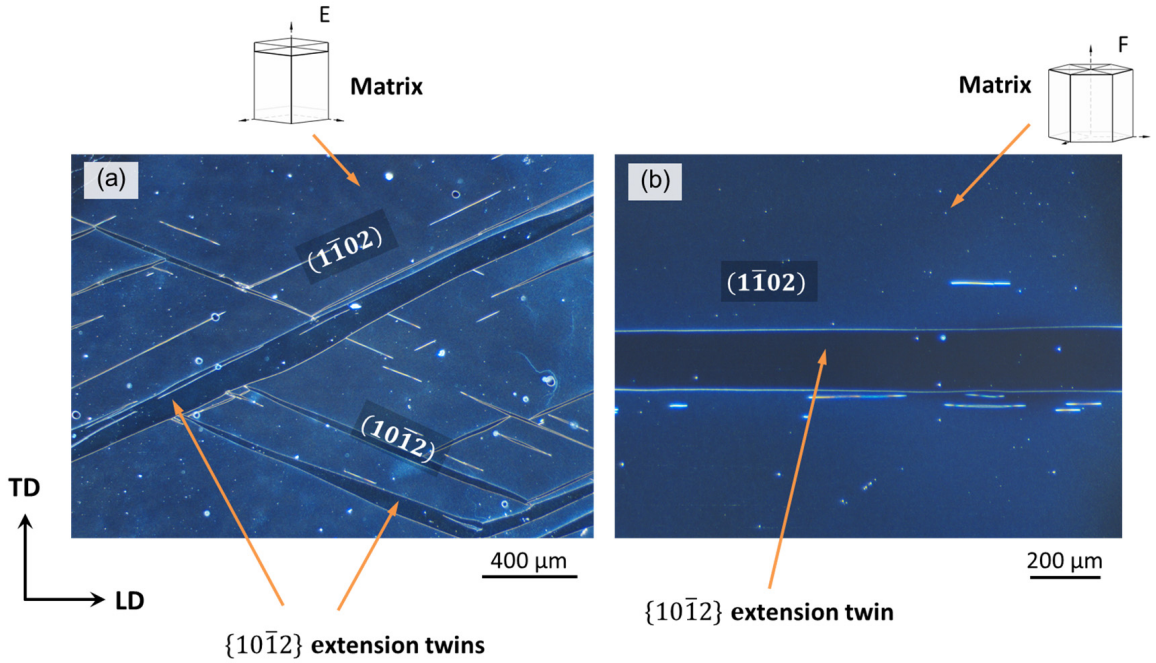

Figure 15. Optical micrographs after PSC tests at room temperature of crystals with (**a**) orientation E and (**b**) orientation F at a true strain of −3% in the initial rapid hardening region in Figure 14.

The orientations of these $\{10\bar{1}2\}$ extension twins are depicted in Figure 16. The orientations of the $\{10\bar{1}2\}$ extension twins in the case of the initial orientation E (orange in Figure 16a) were essentially identical to those in orientation C (Figure 11a), but rotated around CD by 90°. The basal poles (*c*-axes) were nearly at an angle of 30° to CD, yielding a non-zero Schmid factor for basal slip in the twinned volume. The $\{10\bar{1}2\}$ extension twins in orientation F rotated the *c*-axes to be almost parallel to CD. The twin orientations (red in Figure 16b) were practically identical to the starting orientation A, for which basal slip was suppressed. The matrix orientations (green in Figure 16a and blue in Figure 16b) were still identical to the respective starting orientations E and F, i.e., there was no rotation of the matrix around the *c*-axis.

Besides $\{10\bar{1}2\}$ extension twinning, $\{10\bar{1}1\}$ contraction twins were observed to form, originating from $\{10\bar{1}2\}$ extension twin boundaries (Figure 17a). Furthermore, bundles of $\{10\bar{1}1\}$ contraction twins (Figure 17b) crossed the larger $\{10\bar{1}2\}$ extension twins and formed long bands that traversed the entire sample. It was found that the appearance of $\{10\bar{1}1\}$ contraction twins for both orientations E and F coincided with the drop in strain hardening (Figure 14). (For a thorough analysis of the microstructure evolution in specimens with a constrained *c*-axis (orientations E and F) during PSC tests at room as well as elevated temperatures the reader is referred to Ref. [22].)

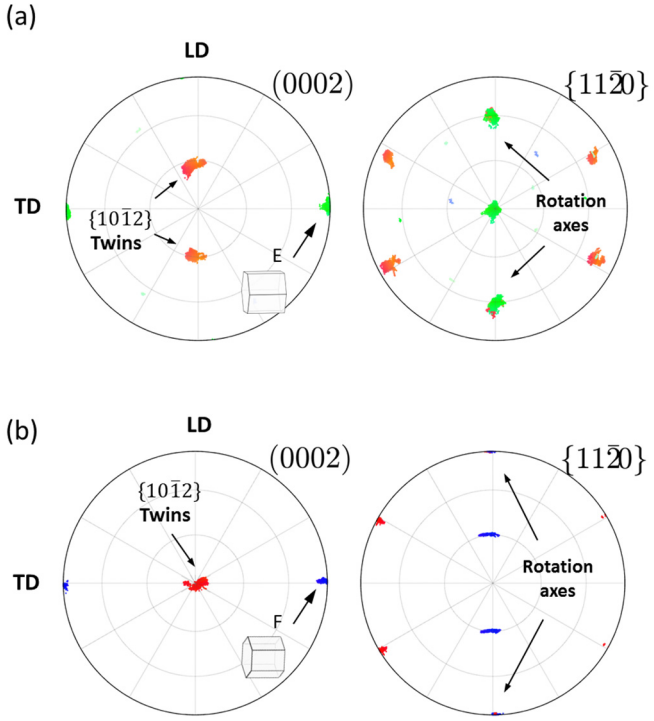

Figure 16. Discrete (scatter) pole figures for specimens with (**a**) orientation E at a true strain of −4.8% and (**b**) orientation F at a true strain of −5.5% obtained by EBSD measurements.

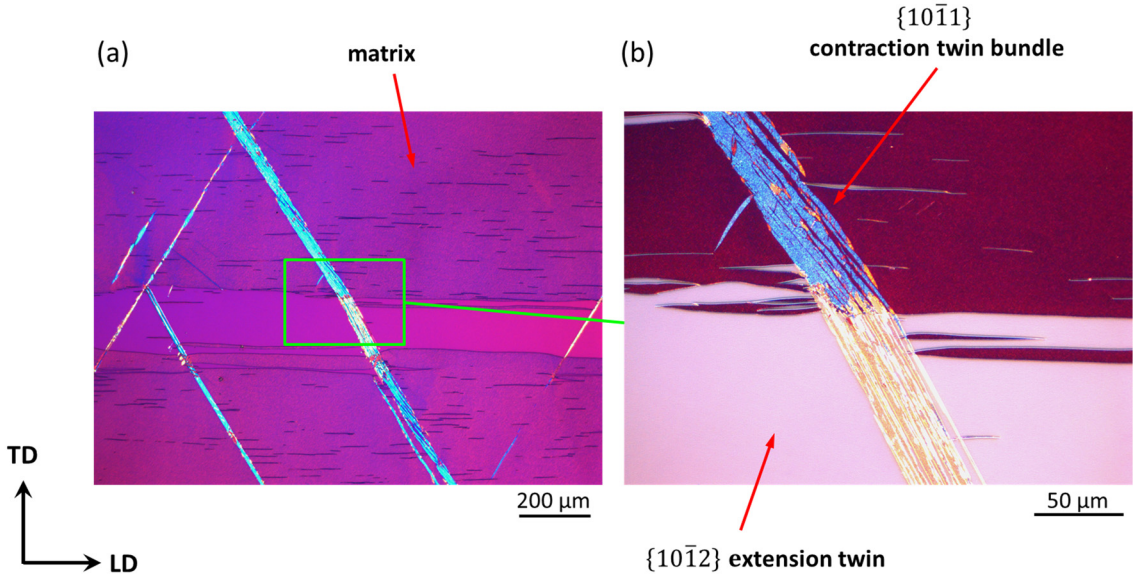

Figure 17. Optical micrographs after PSC tests at room temperature of crystals with orientation F at a true strain of −5.5% after the drop in strain hardening (Figure 14). (**b**) is a magnified view of the center region in (**a**).

3.5. Compression at 45° to the c-Axis (Orientations G and H)

Orientations G and H were specifically aligned for slip on the basal plane. The stress–strain curves are shown in Figure 18. A region of low work hardening was observed during the incipient stage of deformation. Initial linear strain hardening rates were the lowest compared to all other tested orientations with $d\sigma_t/d\varepsilon_t$ of 13.5 MPa and 35 MPa for orientation G and H, respectively.

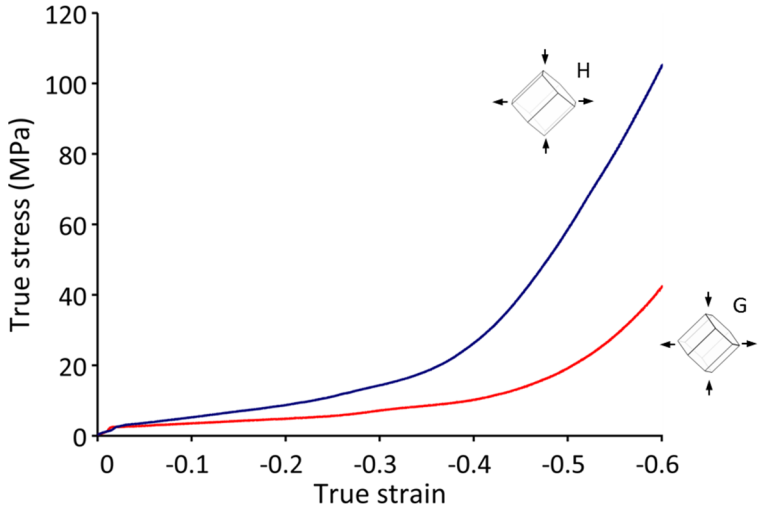

Figure 18. Flow curves of pure Mg single crystals of orientations G and H (45° between CD and the *c*-axis) deformed by PSC at ambient temperature and a constant strain rate of 10^{-3} s^{-1}. Oil was used for lubrication.

However, at higher strains (above −0.3), a significant increase in work hardening was apparent (Figure 18). Nevertheless, specimens of both orientations were deformed up to a true strain of −1 without fracture. Concurrently with the increase in work hardening, bands of $\{10\bar{1}2\}$ extension twins were found to form, although the Schmid factor for extension twinning was negative. The origin and the role of these extension twins was addressed in greater detail in Ref. [23].

4. Deformation Behavior and Failure of Crystals with 'Hard' Orientations

As expected, out of all tested orientations, crystals with the 'hard' basal orientations A and B in *c*-axis compression displayed the least ductile behavior. As mentioned, basal slip was suppressed in this case. However, in the initial rapid work hardening regime, the deformation was already plastic since the highest work hardening rates ($d\sigma_{t,A}/d\varepsilon_{t,A}$ = 6.3 GPa and $d\sigma_{t,B}/d\varepsilon_{t,B}$ = 6.9 GPa for orientation A and B, respectively) were still a fraction of the Young's modulus ($E_{[0001]}$ = 50.8 GPa) in the *c*-axis direction. As discussed in [5,6], a minimal deviation from the exact alignment of the *c*-axis from the compression direction is enough to activate basal slip due to the very low critical resolved shear stress of about 0.5–1.5 MPa [24–34]. The initial strain hardening rate in the case of easy basal slip (orientation G) was determined to be $d\sigma_{t,G}/d\varepsilon_{t,G}$ = 13.5 MPa. The highest Schmid factor for basal slip in orientation G was m_G = 0.5 owing to the alignment of the basal plane at an angle of 45° to the compression direction. Since orientation A and G differed only in the inclination of their *c*-axes with respect to CD, their initial linear strain hardening rates (assuming basal slip only) are related by

$$\frac{d\tau}{d\gamma} = \frac{d\sigma_{t,A}}{d\varepsilon_{t,A}} {m_A}^2 = \frac{d\sigma_{t,G}}{d\varepsilon_{t,G}} {m_G}^2 \quad (1)$$

where $d\tau/d\gamma$ is the basal shear hardening rate, σ_t and ε_t are the true stress and true strain, respectively, with the corresponding orientations denoted as subscript. The Schmid factor for basal slip in the case of orientation A would be $m_A = 0$ ideally. From Equation (1) it follows that $m_A = 0.023$ if the observed initial linear strain hardening rates for the orientations A and G are used. This Schmid factor translates into a deviation of $\Delta\phi = \text{asin}(2m_A)/2 = 1.3^\circ$ from the ideal 'hard' orientation A, which is not unreasonable. However, if the deformation was governed by basal slip only, the *c*-axis would have rotated further towards the compression direction throughout straining, continuously increasing the strain hardening rate $d\sigma_{t,A}/d\varepsilon_{t,A}$. Experimentally, a decrease in strain hardening was

observed in both cases of orientation A and B (Figure 4), which suggests the activation of a different deformation mode.

Slip lines observed in A-oriented crystals were parallel to the trace of $\{11\bar{2}2\}$ planes (Figure 6), indicating the activation of pyramidal II slip. As opposed to basal slip, pyramidal $\langle c+a \rangle$ slip is able to accommodate the plane strain compression (contraction in CD and extension in LD) imposed on the samples and is most likely the reason for the decrease in the strain hardening rate (Figure 4).

Slip lines have also been ascertained in the case of orientation B that could not be a result of basal slip (Figure 7). The broad range of inclinations of the observed slip lines (43–58° to TD) suggests the activation of pyramidal $\langle c+a \rangle$ slip and cross slip between different pyramidal planes. Assuming the activation of pyramidal II slip as in the case of orientation A, a possible slip plane would be $(11\bar{2}2)$ for dislocations with a Burgers vector parallel to $[11\bar{2}3]$. Such dislocations could also glide on the $(10\bar{1}1)$ plane, i.e., constituting pyramidal I slip. The inclinations of the slip traces for glide on $(11\bar{2}2)$ and $(10\bar{1}1)$ would be 39° and 58.4° to TD, respectively, or any angle between that if cross slip is taken into account. This range of inclinations corresponds well to what was observed experimentally.

Despite the activation of pyramidal $\langle c+a \rangle$ slip in crystals of both hard orientations A and B, the specimens failed by cracking along $\{11\bar{2}4\}$ planes (Figure 5). The $\{11\bar{2}4\}$ fracture plane has also been reported previously by Kelley and Hosford [6] for PSC of Mg single crystals as well as by Reed-Hill and Robertson [35] for tension at −190 °C. More recently, the same fracture plane has been observed during equal-channel angular pressing (ECAP) [36] and *c*-axis compression [37,38] of Mg single crystals at room temperature. While both A- and B-oriented specimens failed, the true stress at fracture was higher for orientation B (Figure 4). The $\{11\bar{2}4\}$ fracture planes are illustrated in Figure 19. In the case of orientation A (Figure 19a), the shear stress on the active $\{11\bar{2}4\}$ fracture planes (in a direction parallel to LD) depends only on the active stress component in CD (the $\{11\bar{2}4\}$ planes are parallel to TD). By contrast, the shear stress on the $\{11\bar{2}4\}$ planes resulting from the active stress component in orientation B (Figure 19b) is always reduced by the lateral compressive reaction stress (in TD), which is presumably the reason for the higher fracture stress.

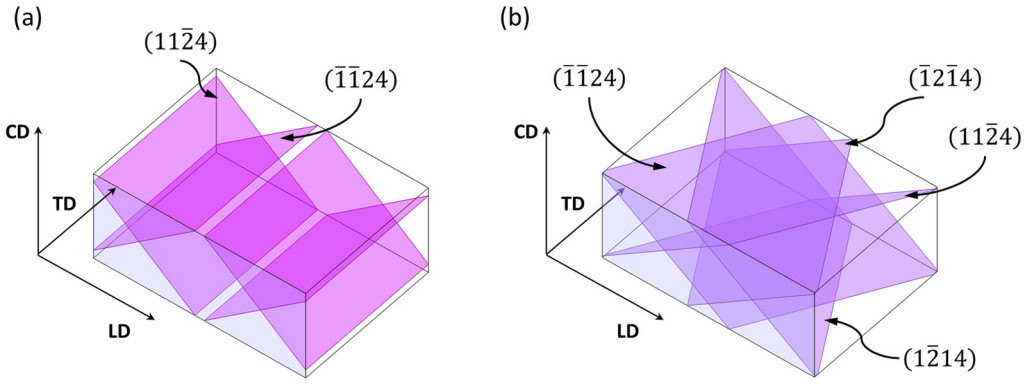

Figure 19. Alignment of $\{11\bar{2}4\}$ fracture planes in specimens of (**a**) orientation A and (**b**) orientation B with respect to the sample reference frame LD-TD-CD.

As mentioned in Section 3.2, cracks and bands of recrystallized grains were evident parallel to the trace of $\{11\bar{2}4\}$ planes (Figure 8). Twins that follow a $\{11\bar{2}4\}$ habit plane were reported by Yoshinaga and Horiuchi [39] and by Kitahara et al. [38] for the case of *c*-axis compression of Mg single crystals. However, the twins in [38] could have been ordinary $\{10\bar{1}2\}$ twins instead of $\{11\bar{2}4\}$ twins since both shared the same inclination (39°) of the twin trace on the observed $\{10\bar{1}0\}$ plane. On the other hand, the horizontal lines that were shown in [38] on the $\{11\bar{2}0\}$ plane were most likely slip traces rather than twin traces. $\{11\bar{2}4\}$ twins have not been ascertained by orientation measurements, neither in [38], nor

in [39]. In the present study no indication of $\{11\bar{2}4\}$ twinning was found, i.e., twinning was not the origin of the recrystallized $\{11\bar{2}4\}$ bands.

Adjacent to the $\{11\bar{2}4\}$ bands, the matrix was rotated away from the initial hard orientation, providing further evidence for the activation of pyramidal slip. The orientations of the recrystallized grains, extracted from the orientation map in Figure 8c, are given in the form of pole figures in Figure 20.

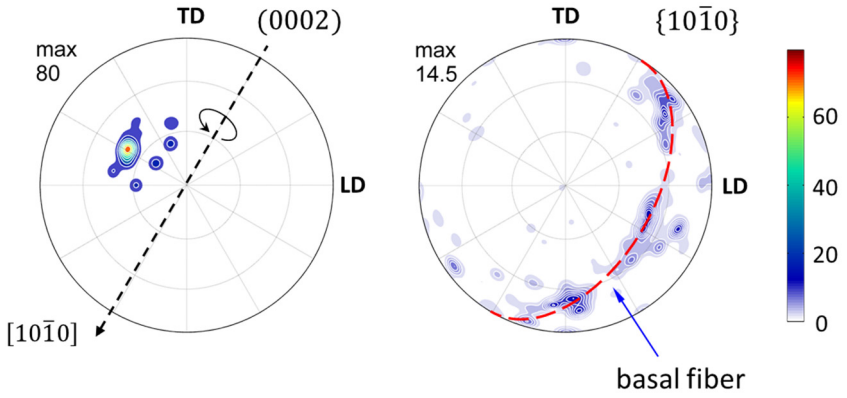

Figure 20. (0002) and $\{10\bar{1}0\}$ pole figures of the recrystallized grains, extracted from the orientation map in Figure 8c.

The *c*-axes were rotated away from the center of the pole figure, i.e., the hard orientation, by up to 40° around the $[10\bar{1}0]$ axis (that was parallel to the band itself). Since $\{11\bar{2}4\}$ twinning can be ruled out, this rotation must be attributed to localized pyramidal $\langle c+a \rangle$ slip. In fact, thin bands orientated close to $\{11\bar{2}4\}$ have been observed by Jensen and Backofen [40] in a zirconium alloy in grains where the deformation was accommodated by $\langle c+a \rangle$ slip. Fracture occurred along such bands of highly localized shear that came about due to thermal softening during slip-band formation [40]. It is suggested that the $\{11\bar{2}4\}$ bands observed in the present study were likewise caused by highly localized shear. However, in the present case of pure Mg, such bands recrystallized dynamically with fracture subsequently occurring in those softened regions along grain boundaries. (The same bands that were not recrystallized were also seen in Mg-0.8 wt.% Gd crystals as was recently reported in [41]. The shear localization/softening was most likely responsible for the drop in flow stress prior to fracture (Figure 4). Further indication of the occurrence of (continuous) dynamic recrystallization in such bands of localized $\langle c+a \rangle$ slip activity is provided by the apparent tendency towards a basal fiber in the band (Figure 20b). As reported and discussed in [21], the formation of a basal fiber, i.e., the rotation of grains around their *c*-axes is a recurring element during the continuous dynamic recrystallization in Mg.

Failure of specimens with the hard orientations A and B was not a result of a limited number of available slip systems, i.e., the absence of pyramidal $\langle c+a \rangle$ slip at room temperature, as is generally believed. Pyramidal slip was very well active at room temperature, but the localization of slip led to an instability in flow, which ultimately caused the fracture along $\{11\bar{2}4\}$ bands, i.e., $\langle c+a \rangle$ slip can be viewed as a mechanism inducing plastic instability, rather than contributing to a homogeneous deformation at ambient temperature. That being said, at elevated temperatures, the specimens deformed without failure during *c*-axis compression [42], aided by the profuse formation of contraction twins (with CDRX inside twin bands) and presumably, a diminishing tendency for slip localization with increasing temperature [43].

5. Impact of $\{10\bar{1}2\}$ Extension Twinning on the Ductility of Mg Single Crystals Subjected to Compression Perpendicular to the *c*-Axis

Specimens of orientation C and D were favorably aligned for $\{10\bar{1}2\}$ extension twinning since extension along the *c*-axis was free to occur in LD. Figure 21 shows basal pole figures depicting the calculated $\{10\bar{1}2\}$ extension twin orientations for the initial specimen orientations C and D. For each starting orientation, six extension twins were possible.

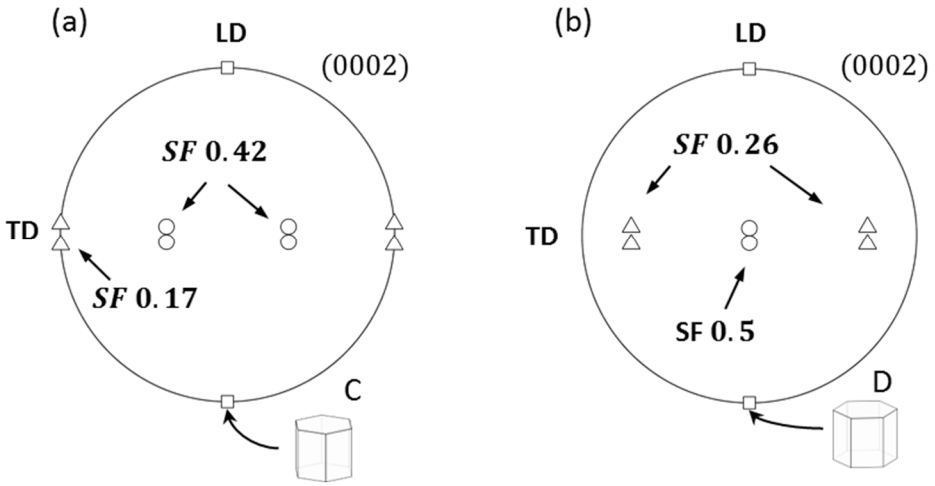

Figure 21. Basal pole figures showing the initial orientations (**a**) C and (**b**) D depicted by squares as well as the corresponding $\{10\bar{1}2\}$ extension twin variants (triangles and circles). Circles indicate the experimentally observed high Schmid factor (SF) twin variants.

Four equally high Schmid factor extension twins in orientation C transformed the matrix into twin orientations with the *c*-axis aligned at an angle of 30° to CD (Figures 11a and 21a), yielding a non-zero Schmid factor ($m = 0.28$) for basal slip as opposed to a zero Schmid factor (ideally) in the case of the starting orientation. The averaged displacement gradient tensor (expressed in the sample reference frame LD-TD-CD) for the four active twin systems is given by (see Appendix in [23])

$$\boldsymbol{e}_C = \begin{pmatrix} 0.0646 & 0 & 0 \\ 0 & -0.0161 & 0 \\ 0 & 0 & -0.0484 \end{pmatrix}$$

Hence, contraction of the *c*-axis due to extension twinning was accompanied by some contraction in TD (negative $\boldsymbol{e}_{C22}$ component). This stage of profuse $\{10\bar{1}2\}$ extension twinning corresponded to the initial low strain hardening region on the flow curve (red curve in Figure 9). The strain hardening rate increased once twinning was exhausted (maximum strain of $\boldsymbol{e}_{C33} = -4.8\%$). It is noted that during the primary twinning stage the flow stress did not remain constant, which means that twinning became more difficult with increasing strain, probably as a consequence of the decreasing residual volume of the parent matrix at strains approaching –4.8%, reflecting the grain size sensitivity of twinning [9,44–46].

That being said, taking into account slip, one would not expect the strain hardening rate to increase after twinning ceases to operate because the Schmid factor for basal slip in the twinned volume is non-zero. However, the deformation produced by basal slip in the twinned volume was resisted by the channel-die constraints. Hence, basal slip was mostly suppressed. Only a small amount of strain could be accommodated by basal slip since extension twinning yielded some contraction in TD ($\boldsymbol{e}_{C22} = -1.6\%$). Thus, the flow stress increased rapidly until $\{10\bar{1}1\}$ contraction twinning was activated, leading to flow softening (Figures 9 and 22) due to intense shear localization and continuous dynamic recrystallization (CDRX) at room temperature (see [21]). The end of the rapid

work hardening stage, slightly before the peak stress on the flow curve in Figure 22, can therefore be correlated with the onset of $\{10\bar{1}1\}$ contraction twinning. Taking into account the Schmid factor for the observed $\{10\bar{1}1\}$ twin variant in the new tension twinned matrix ($m = 0.34$), the CRSS for contraction twinning at room temperature amounts to $\tau_{\{10\bar{1}1\}}$ = 61 MPa, which is well below the range of values (76–154MPa) reported by Wonsiewicz and Backofen [5] for various orientations.

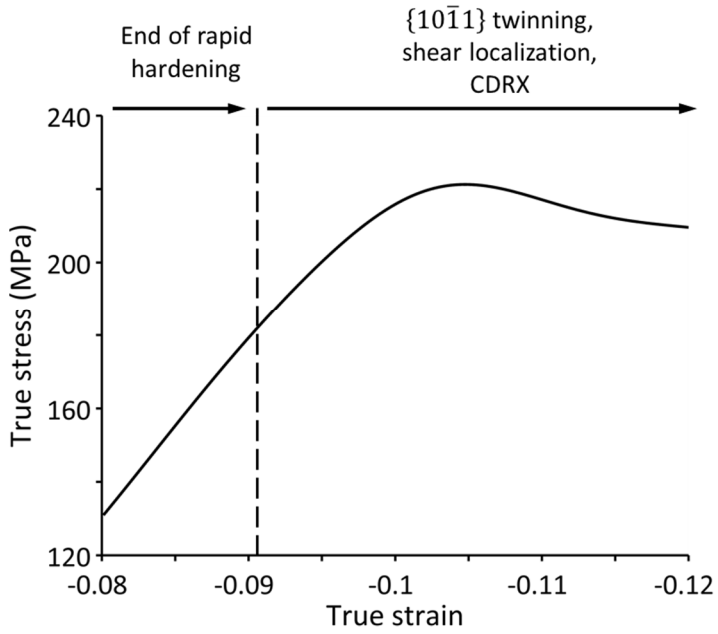

Figure 22. Transition from rapid work hardening to a steady state of C-oriented pure Mg crystals as in Figure 9 (red curve). The curve shown is a Gaussian fit (goodness-of-fit $R^2 = 0.9997$) to the measured data.

In the case of orientation D, two high Schmid factor extension twin variants were observed to appear, which converted the initial matrix into twin orientations located nearly in the center of the basal pole figure (Figures 11b and 21b). Extension twinning was activated at stresses above 4 MPa, which translates into a CRSS of $\tau_{\{10\bar{1}2\}} \approx 2$ MPa and is in good agreement with the CRSS for extension twinning reported by Yu et al. ($\tau_{\{10\bar{1}2\}} = 2.4$ MPa) [47] and Reed-Hill and Robertson ($\tau_{\{10\bar{1}2\}} \approx 2$ MPa) [48].

The averaged displacement gradient tensor (LD-TD-CD reference frame) for the two active twin systems is given by

$$\boldsymbol{e}_D = \begin{pmatrix} 0.0646 & 0 & 0 \\ 0 & 0 & 0 \\ 0 & 0 & -0.0646 \end{pmatrix}$$

Extension twinning in orientation D did not entail any contraction in TD but produced ideal plane strain compression. More strain (contraction in CD) was accommodated by twinning in comparison with orientation C; hence, the initial region of low strain hardening was longer in orientation D (blue curve vs. red curve in Figure 9).

Twinning transformed orientation D into the 'hard' orientation B, the ductility of which was rather limited as discussed in the previous section. Consequently, the strain hardening rate of orientation D became very similar to that of orientation B and specimens fractured at the same stress (Figure 3b).

It is worth pointing out that after the conversion of the initial matrix, specimens with the starting orientation D were again almost single-crystalline with only low angle grain boundaries present, as shown in Figure 13 (parallel to TD), owing to the misorientation relationship of 7.4° $\langle 11\bar{2}0 \rangle$ between the two twin variants. On the other hand, the four

twin variants consuming orientation C introduced high angle grain boundaries, i.e., 60° $\langle 10\bar{1}0 \rangle$ and 60.4° $\langle 8\bar{1}\bar{7}0 \rangle$ [21]. Moreover, in specimens of orientation C secondary extension twins, i.e., 86.3° $\langle 11\bar{2}0 \rangle$ grain boundaries were also present after the conversion of the initial matrix.

In addition to the apparent difference in ductility between the C- and D-oriented crystals, their mechanical behavior during the incipient stage of deformation, i.e., in the stage characterized by large-scale twinning, was distinguished by a higher strain hardening rate in the crystals of orientation C vis-à-vis the D-oriented crystals with 544 MPa and 297 MPa, respectively (Figure 9). The four twin variants that originated from orientation C (Figure 21a) were mutually more constrained, i.e., impeding each other, than the two twin variants from orientation B (Figure 21b), having a virtually identical orientation. As the conversion of the original single crystal orientation was progressing, it became more difficult to twin the "residual" fragmented matrix as smaller grains offer a greater resistance against twinning. The fragmentation of the initial matrix was more distinct in case of orientation C due to the higher number of twin variants, creating smaller pockets of stable retained matrix, thus resulting in a higher strain hardening rate. Moreover, the twins in the C-oriented crystals had to form in pairs of symmetric variants (symmetric about LD) to mutually cancel out their shear components in TD, whereas in the case of orientation D, the twins did not introduce any shear in TD at all, so they could form more easily a priori, which is reflected in the low CRSS of about 2 MPa.

In both cases of orientation C and D, basal slip was effectively suppressed in the twinned volume. However, the deformation behavior was markedly different. The most striking difference was in the appearance of $\{10\bar{1}1\}$ contraction twins in orientation C [21] that were not present in orientation D, although the latter reached a higher flow stress and the *c*-axis was aligned parallel to CD (favorably for contraction twinning). This can be attributed to the presence of high angle grain boundaries in orientation C, which acted as nucleation sites for $\{10\bar{1}1\}$ contraction twins. No such high angle grain boundaries existed in orientation D, but only low angle grain boundaries were present after the conversion by extension twinning, which, however, did not facilitate contraction twinning.

A similar conclusion can be drawn for the case of orientations E and F. The calculated $\{10\bar{1}2\}$ extension twin orientations for these initial orientations are illustrated in Figure 23. Similar to the case of orientations C and D, four variants of extension twins formed in crystals of orientation E (Figure 23a) and two variants formed in crystals of orientation F (Figure 23b). The twin orientations in the E-oriented specimens had a non-zero Schmid factor as in the case of the twin orientations of the C-oriented ones (Figure 21a), but basal slip was not suppressed by the channel-die constraints in the twinned volume.

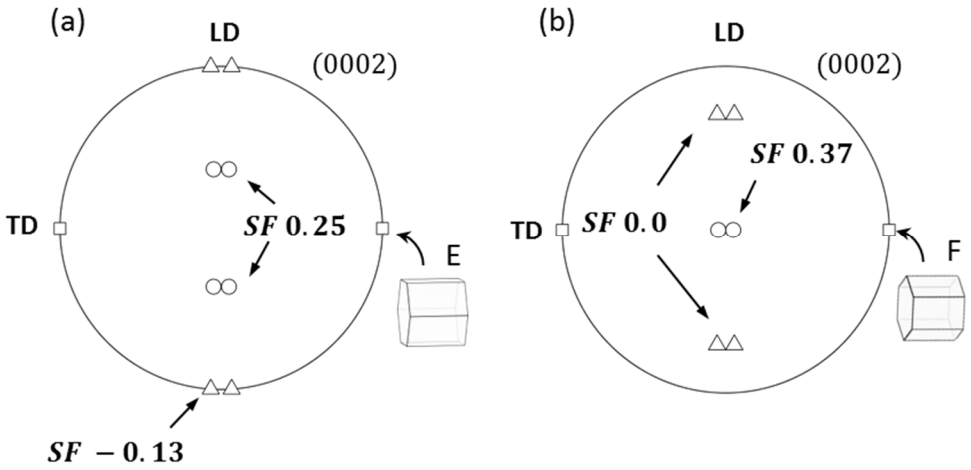

Figure 23. Basal pole figures showing the initial orientations (**a**) E and (**b**) F depicted by squares as well as the corresponding $\{10\bar{1}2\}$ extension twin variants (triangles and circles). Circles indicate the experimentally observed high Schmid factor (SF) twin variants.

The twin orientations in the F-oriented specimens rotated the matrix towards the hard orientation A, in which basal slip was naturally suppressed, which is the reason for the higher flow stress in case of orientation F compared to orientation E (Figure 14). It would seem that fracture under such conditions must have been unavoidable.

Large $\{10\bar{1}2\}$ extension twins formed despite the constrained *c*-axis (Figure 15). However, these twins could not grow to such an extent as to consume the entire matrix, like they did in the case of orientations C and D, i.e., high angle grain boundaries (86.3° $\langle 11\bar{2}0\rangle$ twin boundaries) were still present. Instead, the formation of $\{10\bar{1}2\}$ extension twins increased the compressive constraint stress (in TD), inhibiting their own growth, until $\{10\bar{1}1\}$ contraction twins nucleated at $\{10\bar{1}2\}$ extension twin boundaries (Figure 17) and compensated the *c*-axis extension, while relieving the constraint stress. Such a cooperative twinning was a necessary deformation mechanism in specimens of both orientations E and F to substitute the inactive prismatic slip at room temperature [22].

With respect to prismatic slip, it is noted that if prismatic slip was active, it would have yielded a rotation around the *c*-axis in orientation F (not in orientation E as it is a stable orientation [6,22]). However, no rotation/spin around the *c*-axis was detected; hence, prismatic slip was not activated in the matrix at room temperature under the most geometrically favorable conditions.

If it were not for the *c*-axis constraint and the suppression of extension twinning, crystals of orientation F would have completely converted into single crystals with the hard orientation A and failed as a result. On the other hand, without any extension twins, contraction twins would not have nucleated either. Thus, a microstructure comprising many fine extension twins seems to be most preferable for the formation of $\{10\bar{1}1\}$ contraction twins, which can for instance be achieved by inhibiting the growth of $\{10\bar{1}2\}$ twins through precipitation [49,50].

Concerning the propagation of $\{10\bar{1}2\}$ extension twins, it is noteworthy that these 'profuse' twins grow easily by the migration of their twin interfaces, i.e., shear-coupled grain boundary migration [51]. By contrast, $\{10\bar{1}1\}$ contraction twin bands propagate by nucleation and limited growth of new fine parallel lamellae (Figure 17b), which reflects the difficulty of the migration of $\{10\bar{1}1\}$ twin boundaries under mechanical stress at room temperature.

6. On the Mechanical Response of Crystals with Soft Orientations

The calculated Schmid factors (SF) for basal slip in orientations G and H are listed in Table 2. (For the calculation of the SF in the current study see Appendix A). G-oriented crystals were aligned such that, ideally, only one slip system with the maximum Schmid factor of $m_G = 0.5$ (Table 2) should be activated in order to accommodate the imposed deformation, i.e., the case of easy basal slip. The shear direction $[\bar{2}110]$ for this slip system was perpendicular to TD; that is, basal slip was free to occur. By contrast, in orientation H, two basal slip systems with equally high Schmid factors (Table 2) must be activated, i.e., coplanar slip, to accommodate the strain. Shear along only one of the two shear directions is resisted by the channel-die constraints; hence, both systems must contribute equally to the overall deformation in a cooperative fashion.

Table 2. Schmid factors (SF) for the respective slip directions for basal slip in crystals of orientations G and H.

Slip Direction	SF Orientation G	SF Orientation H
$[\bar{1}2\bar{1}0]$	0.25	0.433
$[\bar{2}\bar{1}10]$	0.5	0.433
$[\bar{1}\bar{1}20]$	0.25	0

The shear stress (τ)–shear strain (γ) curves for orientations G and H are depicted in Figure 24. The critical resolved shear stress for basal slip at RT was determined to be τ_{CRSS} = 1.2 MPa and τ_{CRSS} 1.15 MPa for orientation G and H, respectively, which is less than the CRSS for $\{10\bar{1}0\}$ contraction twinning by a factor of about 50. The reduced shear hardening rate for orientation G in stage A (initial linear hardening stage) is given by $\theta_{r,G} = (d\tau_G/d\gamma_G)/\mu_B = 1.73 \times 10^{-4}$, where μ_B = 16.4 GPa is the shear modulus for basal slip. For comparison, Sułkowski et al. [32] reported a reduced initial (stage A) shear hardening rate of 1.83×10^{-4} for the same orientation deformed in tension, which is close to the value measured in the present work, despite the prevalent friction in channel-die compression. For orientation H, the reduced shear hardening rate (stage A) amounts to $\theta_{r,H} = 4.02 \times 10^{-4}$ (shear direction $[\bar{1}100]$), which is considerably higher than in the case of easy basal slip in orientation G ($\theta_{r,G}$). This increased hardening in orientation H can most probably be attributed to the channel-die constraints and/or to the interaction of basal dislocations with different Burgers vectors, given that a coplanar slip system hardens proportionally to the dislocation density accumulated in the other coplanar system during stage A in magnesium [34].

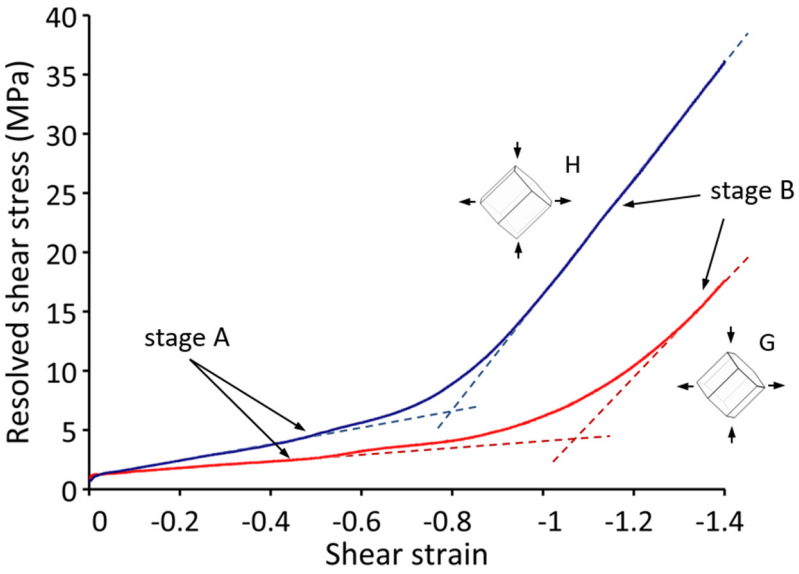

Figure 24. Resolved shear stress–shear strain curves of pure Mg single crystals of orientations G and H (shown up to a shear strain of −1.4) corresponding to the true stress–strain curves in Figure 18.

The reduced shear hardening rates in the rapid work hardening region in Figure 24 were 2.3×10^{-3} and 3.0×10^{-3} for orientation G and H, respectively, which is an order of magnitude greater compared to the initial region of low strain hardening. As was shown in [23], this increase in strain hardening was accompanied by changes in the microstructure, namely, the appearance of $\{10\bar{1}2\}$ extension twin bands that presumably acted as barriers for dislocations slip. The appearance of $\{10\bar{1}2\}$ twins during the rapid hardening stage (stage B) was also observed by Yoshinaga and Horiuchi [28] as well as by Hirsch and Lally [29] on single crystals strained in tension. In the study by Sułkowski et al. [32], the work hardening in stage B was rather moderate (reduced coefficient of 6.71×10^{-4}) compared to the rapid hardening stage in our work for orientation G (2.3×10^{-3}). Twins have not been observed in [32], but the increase in work hardening was associated with the appearance of low angle grain boundaries, i.e., subgrain formation, that reduced the mean dislocation free path.

Thus, there are ample reasons to suggest that, in contrast to fcc crystals, the stage of rapid hardening in Mg is not governed primarily by the interaction of primary dislocations with forest dislocations [52] but rather by actual changes in the microstructure [28].

7. Summary and Concluding Remarks

In this work, an overview is given to comprehensively illustrate the mechanical response and microstructure evolution of specifically oriented pure magnesium single crystals under plane strain compression at room temperature.

Mg crystals of 'hard' orientations that were compressed along the *c*-axis displayed high hardening rates and limited ductility at room temperature, failing at a true strain of about -7%, although pyramidal $\langle c+a \rangle$ slip was readily activated, as ascertained by observation of slip traces and lattice rotation. Fracture occurred along recrystallized bands aligned along $\{11\bar{2}4\}$ crystallographic planes, which were the result of highly localized shear. The failure in *c*-axis contraction at ambient temperature is therefore fostered by a tendency for localization of pyramidal $\langle c+a \rangle$ slip and is of a ductile nature.

In crystals favorably aligned for *c*-axis extension, profuse $\{10\bar{1}2\}$ extension twins, forming massively in the early stages of deformation, consumed the entire crystal, leaving no trace of the original matrix, which demonstrates the ease of nucleation and growth potential of extension twins. The dominant $\{10\bar{1}2\}$ extension twins corresponded to high Schmid factor twin variants in both cases of compression along $\langle 11\bar{2}0 \rangle$ as well as $\langle 10\bar{1}0 \rangle$ crystallographic directions. In both cases, basal slip was effectively suppressed in the twinned volume. The deformation behavior of the differently oriented crystals, however, was remarkably different. $\{10\bar{1}2\}$ extension twinning during compression along $\langle 10\bar{1}0 \rangle$ resulted in a microstructure effectively comprising one single orientation (single crystal) with the *c*-axis becoming parallel to the compression direction, i.e., twinning produced a single crystal of a 'hard' orientation. Preventing the formation of such a 'hard' texture component by promoting low Schmid factor twin variants is vital in order to improve the room temperature ductility. By contrast, in compression along $\langle 11\bar{2}0 \rangle$, exceptionally high room temperature ductility can be achieved. Considering the microstructure evolution, the decisive difference was in the appearance of $\{10\bar{1}1\}$ contraction twins in the latter case, which were not present in the former. Subsequently, substantial weakening of the texture was attained by multiple generations of extension/contraction twins and the occurrence of dynamic recrystallization inside contraction twin bands. The formation of a hard basal texture component that is associated with poor room temperature ductility was therefore fully suppressed (for more details, see [21]).

The formation of $\{10\bar{1}2\}$ extension twins could not be prevented by the channel-die constraints when *c*-axis extension was confined; however, growth of this 'profuse' twin type was very well inhibited. The presence of high angle grain boundaries and, in particular, $\{10\bar{1}2\}$ twin boundaries was found to be a prerequisite for the activation of $\{10\bar{1}1\}$ contraction twinning by providing nucleation sites for the latter.

Prismatic slip was not found to operate at room temperature in the case of starting orientations most favorably aligned for prismatic slip; instead, cooperative $\{10\bar{1}2\}$ extension and $\{10\bar{1}1\}$ contraction twinning was activated (for more details see [22]).

Deformation of crystals with 'soft' orientations that were favorably oriented for easy basal and coplanar basal slip, respectively, was characterized by a long initial region of low work hardening (stage A). The reduced shear hardening rates were 1.73×10^{-4} and 4.02×10^{-4} for easy basal slip and coplanar slip, respectively. The low work hardening region (stage A) of easy basal slip and coplanar basal slip gradually transitioned into a region of rapid work hardening (stage B) with shear rates that were an order of magnitude greater compared to stage A. The increase in work hardening in stage B was attributed to changes in the microstructure rather than the interaction of primary dislocations with forest dislocations.

Author Contributions: Conceptualization, T.A.-S. and D.A.M.; methodology, K.D.M.; software, K.D.M.; validation, K.D.M., T.A.-S. and D.A.M.; formal analysis, K.D.M., T.A.-S. and D.A.M.; investigation, K.D.M.; data curation, K.D.M.; writing—original draft preparation, K.D.M.; writing—review and editing, T.A.-S. and D.A.M.; supervision, D.A.M.; project administration, T.A.-S.; funding acquisition, T.A.-S. All authors have read and agreed to the published version of the manuscript.

Funding: This research was funded by the Deutsche Forschungsgemeinschaft (DFG), grant number AL1343/5-1.

Data Availability Statement: The data required to reproduce these findings cannot be shared at this time due to the legal or ethical reasons.

Conflicts of Interest: The authors declare no conflict of interest.

Appendix A. Calculation of the Schmid Factor for Slip and Twinning in Channel-Die PSC

The SFs have been calculated assuming a stress tensor with compressive stresses σ and σ/κ parallel to CD and TD, respectively, where κ is the ratio between the active and reaction stresses. For a given starting orientation of a single crystal, the ratio κ can be readily calculated under the condition of zero strain ($\varepsilon_{yy} = 0$) in TD, assuming, to a first approximation, that the orientation-dependent elastic lateral compliance determines the constraint stress [53,54], at least during the onset of deformation. The resolved shear stress in a given slip or twinning system is given by:

$$\tau_{RSS} = m_a \times \sigma + m_r \times \frac{\sigma}{\kappa} \tag{A1}$$

where m_a is the SF associated with the active stress in CD and m_r is the SF associated with the reaction stress in TD. In order to formulate a SF that depends solely on the active stress component σ of the biaxial stress state, both m_a and m_r can be combined:

$$\tau_{RSS} = \left(m_a + \frac{m_r}{\kappa}\right) \times \sigma = m \times \sigma \tag{A2}$$

with the Schmid factor $m = (m_a + m_r/\kappa)$. For ideal plastic behavior, $\kappa = 2$. For basal slip in the case of orientation G and H, it holds that $m = m_a$ since $m_r = 0$.

The calculated κ ratios are given in Table A1 for the investigated initial orientations of the single crystals. The κ ratios are identical for orientations that share a rotation around the *c*-axis due to the infinite order of rotational symmetry of the Young's modulus around the *c*-axis (Figure A1). The elastic stiffness tensor for Mg that was used in this work was taken from [55].

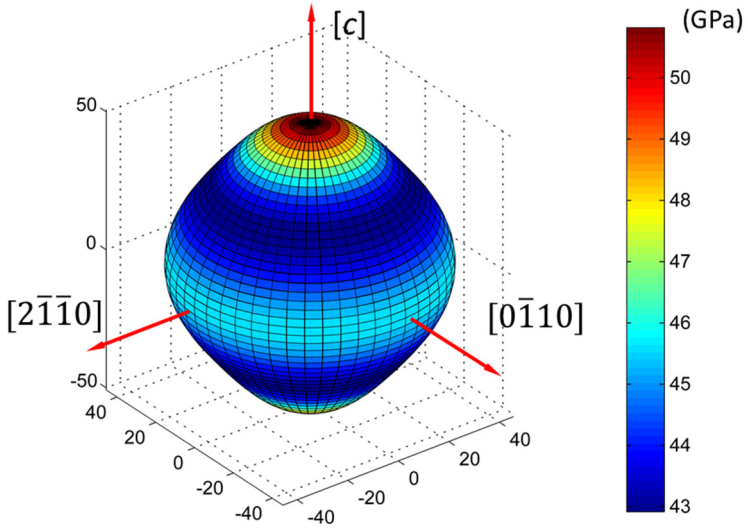

Figure A1. 3D plot of the directional dependence of the Young's modulus of Mg.

Table A1. Calculated stress ratio κ between the active (in CD) and reaction (in TD) stress components of the biaxial stress state in channel-die compression for various tested single crystal orientations and the Euler angles defining the basal fiber for which the respective κ ratio is constant.

Single Crystal Orientation	Basal Fiber	Stress Ratio κ
A, B	$(0°, 0°, \varphi_2)$	4.42
C, D	$(90°, 90°, \varphi_2)$	2.86
E, F	$(0°, 90°, \varphi_2)$	3.97
G, H	$(90°, 45°, \varphi_2)$	3.47

References

1. Bräunig, S.; Düring, M.S.; Hartmann, H.M.; Viehweger, B.H. Magnesium sheets for industrial application. In *Magnesium, Proceedings of the 6th International Conference Magnesium Alloys and Their Applications*; Kainer, K.U., Ed.; Wiley-VCH: Weinheim, Germany, 2005; pp. 955–961.
2. Luo, A.A.; Sachdev, A.K. Applications of magnesium alloys in automotive engineering. In *Advances in Wrought Magnesium Alloys. Fundamentals of Processing, Properties and Applications*; Bettles, C., Barnett, M., Eds.; Woodhead Publishing: Cambridge, UK, 2012; pp. 393–426.
3. Ball, E.; Prangnell, P. Tensile-compressive yield asymmetries in high strength wrought magnesium alloys. *Scr. Metall. Et Mater.* **1994**, *31*, 111–116. [CrossRef]
4. Pekguleryuz, M.O. Current developments in wrought magnesium alloys. In *Advances in Wrought Magnesium Alloys. Fundamentals of Processing, Properties and Applications*; Bettles, C., Barnett, M., Eds.; Woodhead Publishing: Cambridge, UK, 2012; pp. 3–62.
5. Wonsiewicz, B.C.; Backofen, W.A. Plasticity of magnesium crystals. *Trans. AIME* **1967**, *239*, 1422–1431.
6. Kelley, E.W.; Hosford, W.F. Plane-Strain Compression of Magnesium and Magnesium Alloy Crystals. *Trans. Met. Soc. AIME* **1968**, *242*, 5.
7. Gottstein, G.; Zabardjadi, D.; Mecking, H. Dynamic recrystallization in tension-deformed copper single crystals. *Met. Sci.* **1979**, *13*, 223–227. [CrossRef]
8. Männel, P.; Hötzsch, G. On the problem of an average orientation factor for hexagonal metals. *Phys. Status Solidi A* **1971**, *6*, 597–604. [CrossRef]
9. Reh, B.; Hötzsch, G.; Günther, F. Einfluß der mechanischen Zwillingsbildung auf die plastische Verformung von Magnesium-und Magnesium-Cadmium-Vielkristallen. *Krist. Tech.* **1973**, *8*, 337–354. [CrossRef]
10. Barnett, M.R.; Keshavarz, Z.; Ma, X. A semianalytical sachs model for the flow stress of a magnesium alloy. *Metall. Mater. Trans. A* **2006**, *37*, 2283–2293. [CrossRef]
11. Molodov, K.D.; Al-Samman, T.; Molodov, D.A.; Gottstein, G. On the ductility of magnesium single crystals at ambient temperature. *Metall. Mater. Trans. A* **2014**, *45*, 3275–3281. [CrossRef]
12. Molodov, K.D.; Al-Samman, T.; Molodov, D.A. On the diversity of the plastic response of magnesium in plane strain compression. *Mater. Sci. Eng. A* **2016**, *651*, 63–68. [CrossRef]
13. Ho, K.H.; Newman, S.T. State of the art electrical discharge machining (EDM). *Int. J. Mach. Tools Manuf.* **2003**, *43*, 1287–1300. [CrossRef]
14. Bridgman, P.W. Certain Physical Properties of Single Crystals of Tungsten, Antimony, Bismuth, Tellurium, Cadmium, Zinc, and Tin. *Proc. Am. Acad. Arts Sci.* **1925**, *60*, 305–383. [CrossRef]
15. Molodov, D.A.; Ivanov, V.A.; Gottstein, G. Low angle tilt boundary migration coupled to shear deformation. *Acta Mater.* **2007**, *55*, 1843–1848. [CrossRef]
16. Danz, R.; Gretscher, P. C–DIC: A new microscopy method for rational study of phase structures in incident light arrangement. *Thin Solid Films* **2004**, *462–463*, 257–262. [CrossRef]
17. Lowe, D.G. Distinctive Image Features from Scale-Invariant Keypoints. *Int. J. Comput. Vis.* **2004**, *60*, 91–110. [CrossRef]
18. Bachmann, F.; Hielscher, R.; Schaeben, H. Texture Analysis with MTEX—Free and Open Source Software Toolbox. *Solid State Phenom.* **2010**, *160*, 63–68. [CrossRef]
19. Bachmann, F.; Hielscher, R.; Schaeben, H. Grain detection from 2d and 3d EBSD data—Specification of the MTEX algorithm. *Ultramicroscopy* **2011**, *111*, 1720–1733. [CrossRef]
20. Syed, B.; Geng, J.; Mishra, R.K.; Kumar, K.S. [0001] Compression response at room temperature of single-crystal magnesium. *Scr. Mater.* **2012**, *67*, 700–703. [CrossRef]
21. Molodov, K.D.; Al-Samman, T.; Molodov, D.A.; Gottstein, G. Mechanisms of exceptional ductility of magnesium single crystal during deformation at room temperature: Multiple twinning and dynamic recrystallization. *Acta Mater.* **2014**, *76*, 314–330. [CrossRef]
22. Molodov, K.D.; Al-Samman, T.; Molodov, D.A. Cooperative {10–12}/{10–11} twinning and prismatic slip in magnesium crystals. *Materialia* **2021**, *20*, 101210. [CrossRef]

23. Molodov, K.D.; Al-Samman, T.; Molodov, D.A.; Gottstein, G. On the role of anomalous twinning in the plasticity of magnesium. *Acta Mater.* **2016**, *103*, 711–723. [CrossRef]
24. Siebel, G. Physikalische Eigenschaften des Magnesium-Einkristalls und ihre Bedeutung für den Vielkristall. In *Magnesium und Seine Legierungen*; Altwicker, H., Bauer, A., Beck, A., Bohner, H., Buchmann, W., Fiedler, R., Gossrau, G., Keinert, O., Menzen, P., Moschel, W., et al., Eds.; Springer: Berlin/Heidelberg, Germany, 1939; pp. 18–36.
25. Burke, E.C.; Hibbard, W.R. Plastic deformation of magnesium single crystals. *Trans. AIME* **1952**, *194*, 295–303. [CrossRef]
26. Basinski, Z.S. The influence of temperature and strain rate on the flow stress of magnesium single crystals. *Aust. J. Phys.* **1960**, *13*, 284–298. [CrossRef]
27. Sheely, W.F.; Nash, R.R. Mechanical properties of magnesium monocrystals. *Trans. Am. Inst. Min. Metall. Eng.* **1960**, *218*, 416–423.
28. Yoshinaga, H.; Horiuchi, R. Work Hardening Characteristics of the Basal Slip of Magnesium Single Crystals. *Trans. JIM* **1962**, *3*, 220–226. [CrossRef]
29. Hirsch, P.B.; Lally, J.S. The deformation of magnesium single crystals. *Philos. Mag.* **1965**, *12*, 595–648. [CrossRef]
30. Akhtar, A.; Teghtsoonian, E. Solid solution strengthening of magnesium single crystals—I alloying behaviour in basal slip. *Acta Metall.* **1969**, *17*, 1339–1349. [CrossRef]
31. Bhattacharya, B.; Niewczas, M. Work-hardening behaviour of Mg single crystals oriented for basal slip. *Philos. Mag.* **2011**, *91*, 2227–2247. [CrossRef]
32. Sułkowski, B.; Chulist, R.; Beausir, B.; Skrotzki, W.; Mikułowski, B. Stage B work-hardening of magnesium single crystals. *Cryst. Res. Technol.* **2011**, *46*, 439–442. [CrossRef]
33. Chapuis, A.; Driver, J.H. Temperature dependency of slip and twinning in plane strain compressed magnesium single crystals. *Acta Mater.* **2011**, *59*, 1986–1994. [CrossRef]
34. Hiura, F.; Niewczas, M. Latent hardening effect under self- and coplanar dislocation interactions in Mg single crystals. *Scr. Mater.* **2015**, *106*, 17–20. [CrossRef]
35. Reed-Hill, R.E.; Robertson, W.D. The crystallographic characteristics of fracture in magnesium single crystals. *Acta Metall.* **1957**, *5*, 728–737. [CrossRef]
36. Kitahara, H.; Maruno, F.; Tsushida, M.; Ando, S. Deformation behavior of Mg single crystals during a single ECAP pass at room temperature. *Mater. Sci. Eng. A* **2014**, *590*, 274–280. [CrossRef]
37. Ando, S.; Tsushida, M.; Kitahara, H. Deformation Behavior of Magnesium Single Crystal in *c*-Axis Compression and a-Axis Tension. *Mater. Sci. Forum* **2010**, *654*, 699–702. [CrossRef]
38. Kitahara, T.; Ando, S.; Tsushida, M.; Kitahara, H.; Tonda, H. Deformation behavior of magnesium single crystals in *c*-axis compression. *Key Eng. Mater.* **2007**, *345*, 129–132. [CrossRef]
39. Yoshinaga, H.; Horiuchi, R. Deformation Mechanisms in Magnesium Single Crystals Compressed in the Direction Parallel to Hexagonal Axis. *Trans. JIM* **1963**, *4*, 1–8. [CrossRef]
40. Jensen, J.A.; Backofen, W.A. Deformation and fracture of alpha zirconium alloys. *Can. Metall. Q.* **1972**, *11*, 39–51. [CrossRef]
41. Molodov, K.D.; Al-Samman, T.; Molodov, D.A. Impact of gadolinium on deformation and recrystallization behavior of magnesium crystals. *Acta Mater.* **2022**, *240*, 118312. [CrossRef]
42. Al-Samman, T.; Molodov, K.D.; Molodov, D.A.; Gottstein, G.; Suwas, S. Softening and dynamic recrystallization in magnesium single crystals during *c*-axis compression. *Acta Mater.* **2012**, *60*, 537–545. [CrossRef]
43. Sagapuram, D.; Efe, M.; Trumble, K.P.; Chandrasekar, S. Flow transitions and flow localization in large-strain deformation of magnesium alloy. *Mater. Sci. Eng. A* **2016**, *659*, 295–305. [CrossRef]
44. Armstrong, R.W.; Worthington, P.J. A Constitutive Relation for Deformation Twinning in Body Centered Cubic Metals. In *Metallurgical Effects at High Strain Rates*; Rohde, R.W., Butcher, B.M., Holland, J.R., Karnes, C.H., Eds.; Springer: Boston, MA, USA, 1973; pp. 401–414.
45. Meyers, M.A.; Vöhringer, O.; Lubarda, V.A. The onset of twinning in metals: A constitutive description. *Acta Mater.* **2001**, *49*, 4025–4039. [CrossRef]
46. Barnett, M.R.; Keshavarz, Z.; Beer, A.G.; Atwell, D. Influence of grain size on the compressive deformation of wrought Mg–3Al–1Zn. *Acta Mater.* **2004**, *52*, 5093–5103. [CrossRef]
47. Yu, Q.; Zhang, J.; Jiang, Y. Direct observation of twinning–detwinning–retwinning on magnesium single crystal subjected to strain-controlled cyclic tension–compression in [0 0 0 1] direction. *Philos. Mag. Lett.* **2011**, *91*, 757–765. [CrossRef]
48. Reed-Hill, R.E.; Robertson, W.D. Additional modes of deformation twinning in magnesium. *Acta Metall.* **1957**, *5*, 717–727. [CrossRef]
49. Stanford, N.; Barnett, M.R. Effect of particles on the formation of deformation twins in a magnesium-based alloy. *Mater. Sci. Eng. A* **2009**, *516*, 226–234. [CrossRef]
50. Robson, J.D.; Stanford, N.; Barnett, M.R. Effect of particles in promoting twin nucleation in a Mg–5 wt.% Zn alloy. *Scr. Mater.* **2010**, *63*, 823–826. [CrossRef]
51. Molodov, K.D.; Al-Samman, T.; Molodov, D.A.; Korte-Kerzel, S. On the twinning shear of {10–12} twins in magnesium—Experimental determination and formal description. *Acta Mater.* **2017**, *134*, 267–273. [CrossRef]
52. Jackson, P.J.; Basinski, Z.S. Latent hardening and the flow stress in copper single crystals. *Can. J. Phys.* **1967**, *45*, 707–735. [CrossRef]

53. Sue, P.L.; Havner, K.S. Theoretical Analysis of the channel die compression test—1. General considerations and finite deformation of f.c.c. crystals in stable lattice orientations. *J. Mech. Phys. Solids* **1984**, *32*, 417–442. [CrossRef]
54. Havner, K.S.; Sue, P.L. Theoretical Analysis of the channel die compression test—II. First- and second-order analysis of the orientation [110][00-1][-110] in F.C.C. Crystals. *J. Mech. Phys. Solids* **1985**, *33*, 285–313. [CrossRef]
55. Simmons, G.; Wang, H. *Single Crystal Elastic Constants and Calculated Aggregate Properties: A Handbook*; M.I.T. Press: Cambridge, MA, USA, 1971.